

Wireless, closed-loop, smart bandage with integrated sensors and stimulators for advanced wound care and accelerated healing

Received: 11 November 2021

Accepted: 23 September 2022

Published online: 24 November 2022

 Check for updates

Yuanwen Jiang^{1,9}, Artem A. Trotsuk^{2,7,9}, Simiao Niu^{1,9}, Dominic Henn², Kellen Chen^{1,9}, Chien-Chung Shih¹, Madelyn R. Larson², Alana M. Mermin-Bunnell², Smiti Mittal², Jian-Cheng Lai¹, Aref Saberi¹, Ethan Beard², Serena Jing², Donglai Zhong¹, Sydney R. Steele², Kefan Sun¹, Tanish Jain², Eric Zhao¹, Christopher R. Neimeth², Willian G. Viana³, Jing Tang^{1,8}, Dharshan Sivaraj^{2,7}, Jagannath Padmanabhan¹, Melanie Rodrigues², David P. Perrault², Arhana Chattopadhyay², Zeshaan N. Maan², Melissa C. Leeolou², Clark A. Bonham², Sun Hyung Kwon², Hudson C. Kussie^{2,7}, Katharina S. Fischer^{2,7}, Gurupranav Gurusankar¹, Kui Liang¹, Kailiang Zhang⁴, Ronjon Nag¹, Michael P. Snyder¹, Michael Januszyk², Geoffrey C. Gurtner^{2,7}✉ & Zhenan Bao¹✉

'Smart' bandages based on multimodal wearable devices could enable real-time physiological monitoring and active intervention to promote healing of chronic wounds. However, there has been limited development in incorporation of both sensors and stimulators for the current smart bandage technologies. Additionally, while adhesive electrodes are essential for robust signal transduction, detachment of existing adhesive dressings can lead to secondary damage to delicate wound tissues without switchable adhesion. Here we overcome these issues by developing a flexible bioelectronic system consisting of wirelessly powered, closed-loop sensing and stimulation circuits with skin-interfacing hydrogel electrodes capable of on-demand adhesion and detachment. In mice, we demonstrate that our wound care system can continuously monitor skin impedance and temperature and deliver electrical stimulation in response to the wound environment. Across preclinical wound models, the treatment group healed ~25% more rapidly and with ~50% enhancement in dermal remodeling compared with control. Further, we observed activation of proregenerative genes in monocyte and macrophage cell populations, which may enhance tissue regeneration, neovascularization and dermal recovery.

Chronic nonhealing wounds represent a substantial healthcare burden, with >6 million individuals affected in the United States alone¹. A chronic wound is defined as one that has failed to heal by 8–12 weeks and is unable to restore function and anatomical integrity to the

affected site². These wounds are associated with loss of function and mobility, increased social stress and isolation, depression and anxiety, prolonged hospitalization and overall increased morbidity and mortality. In addition, the financial cost to the healthcare system for

the management of chronic wound-related complications has been estimated at >US\$25 billion annually¹.

In normal wound healing, when an injury occurs, the tissue undergoes three canonical stages of wound regeneration: inflammation, new tissue formation and remodeling³. During each stage, different cells are recruited, migrate, become activated and proliferate to achieve tissue regeneration and reduce infection⁴. When this carefully orchestrated process is impaired, there is often not a single cause, but rather multiple factors that contribute. These factors include comorbidities such as diabetes, infection, ischemia, metabolic conditions, immunosuppression and radiation, which can result in high levels of proteases, elevated inflammatory markers, low growth factor activity and reduced cellular proliferation within the wound bed. This can lead to severe patient discomfort and increased hospitalization rates^{5,6}.

While interventions for chronic wounds exist, such as growth factors, extracellular matrix, engineered skin and negative-pressure wound therapy, these treatments are only moderately effective^{6,7}. Current standard-of-care wound dressings are passive and do not actively respond to variations in the wound environment. Smart bandage technologies are well positioned to address these challenges, with their ability to integrate multimodal sensors and stimulators for real-time monitoring and active wound care treatment with minimal physician intervention^{8–14}.

Previous research has demonstrated that as a wound heals, skin impedance increases¹⁵. When a wound becomes infected, however, wound impedance would decrease due to the development of biofilm¹⁶. As the infection develops further, local inflammation increases wound temperature¹⁷. Both signals can be easily captured by low-cost sensors embedded in a wearable device to act as a sentinel for impending wound infection. These biophysical signals provide rapid, robust and accurate information about wound conditions in real time, creating an opportunity to diagnose and monitor a nonhealing wound quickly and autonomously in a closed-loop fashion.

Current smart bandage technologies have demonstrated promise in their ability to sense physiological conditions. This includes detection of pH^{18,19}, temperature^{20–23}, oxygenation²⁴, impedance^{15,25,26}, motion^{27,28} and enzymatic fluctuations^{23,29,30} of the wound. It has also been well established that electrical stimulation can reduce bacterial colonization and biofilm infection and restore normal wound healing *in vivo*³¹. Moreover, electrical stimulation has also been shown to improve tissue perfusion, stimulate immune cell function and accelerate keratinocyte migration through a process known as galvanotaxis^{32–34}. Unfortunately, current electrical stimulation devices are bulky, tethered by wires and uncomfortable to wear, limiting patient compliance. Although recent attempts have tried to generate electric fields by mechanical motion and subsequently accelerate wound healing using nanogenerator devices^{10,11}, there have been limited advancements in the incorporation of both sensing and electrical stimulation technologies to simultaneously deliver active wound care (Supplementary Table 1). Additionally, random mechanical movements cannot guarantee controllable stimulation conditions for consistent treatment. Further, metal-based electrodes without proper tissue adhesion cannot ensure robust device operation in the complex wound environment. As a result, there remains a need to develop portable, autonomous, inexpensive devices to improve wound care.

For improved therapeutic outcomes, an ideal smart bandage platform needs to meet the following requirements. First, it needs to be flexible and wirelessly operated to avoid any undesired tethering and discomfort caused by conventional rigid devices. Next, it should integrate both sensing and stimulation modalities for autonomous, closed-loop wound management. Finally, it should have on-demand skin adhesion with a tight interface for robust signal transduction and energy delivery during operation while also providing easy detachment to avoid possible secondary skin damage during device removal.

To address these requirements, we developed a battery-free flexible bioelectronic system consisting of wirelessly powered sensing and stimulation circuits with tissue-interfacing tough hydrogel electrodes using a biocompatible conducting polymer. We anticipate that this smart bandage will improve therapeutic outcomes and provide new knowledge for wound care.

Specifically, we designed a miniaturized flexible printed circuit board (FPCB) containing an energy-harvesting antenna, a microcontroller unit, a crystal oscillator and filter circuits for dual-channel continuous sensing of wound impedance and temperature, as well as a parallel stimulation circuit to deliver programmed electrical cues for accelerated wound healing. To ensure efficient signal exchange and energy delivery between the circuits and the soft skin tissue, we designed a low-impedance and adhesive hydrogel electrode based on poly(3,4-ethylenedioxythiophene):polystyrene sulfonate (PEDOT:PSS). Compared with well-established ionically conducting hydrogels, our dual-conducting (that is, both electrically and ionically conductive) hydrogel has lower impedance across the entire frequency domain, giving rise to more efficient charge injection during stimulation^{35,36}. To mitigate secondary skin damage when peeling off the adhesive electrodes, we introduced a thermally controlled reversible phase transition mechanism to the hydrogel backbone and achieved two orders of magnitude lower adhesion at elevated temperature when compared with normal skin temperature. Using multiple preclinical animal models, we found that our smart bandage could continuously monitor skin physiological signals and deliver directional electrical cues, leading to accelerated wound closure, increased neovascularization and enhanced dermal recovery. Finally, the wireless nature of our smart bandage allowed us to utilize complex animal models, such as parabiosis, to investigate the possible underlying mechanisms behind the observed effect of electrical stimulation. Our data suggest that the beneficial wound-healing outcomes could be attributed to the activation of proregenerative genes in the monocyte and macrophage cell populations.

Results and discussions

System overview

Our integrated wound management system consists of a battery-free, wirelessly powered FPCB for simultaneous wound treatment and monitoring, as well as a tissue-interfacing conducting adhesive hydrogel interface for robust and gentle skin integration (Fig. 1a,b). Due to the thin layout of the FPCB (~100 µm board thickness) and low modulus of the gel interface, the smart bandage is flexible and can be comfortably attached to wound surfaces (Fig. 1c–e). With an antenna coil that resonates at 13.56 MHz, our smart bandage can be inductively coupled with an external radiofrequency identification (RFID) reader. Through the radiofrequency (RF) energy-harvesting process, the antenna can provide power to apply electric bias across the wound for programmed treatment and, at the same time, drive the microcontroller unit (MCU) and other integrated circuits (for example, oscillator and filter) for continuous monitoring of wound impedance and temperature via a near-field communication (NFC) transponder in the MCU under the ISO 15693 protocol (Figs. 1f and 2a).

Wireless circuit design

For the wireless antenna, we designed a five-turn coil with an optimum inductance of ~1.5 µH, offering a high RF-harvested voltage and wide tunability to reach a resonant frequency of 13.56 MHz for maximized wireless communication signal gain (Fig. 2a–c and Supplementary Fig. 1). Additionally, the quality factor (*Q*) of the antenna is ~18, which strikes the balance between energy-harvesting efficiency and wireless communication bandwidth (Fig. 2b). As a result, our antenna offers a wide and stable 15-cm wireless communication distance (Fig. 2c,d). Our device function also remained stable upon bending (Fig. 2e and Supplementary Fig. 3).

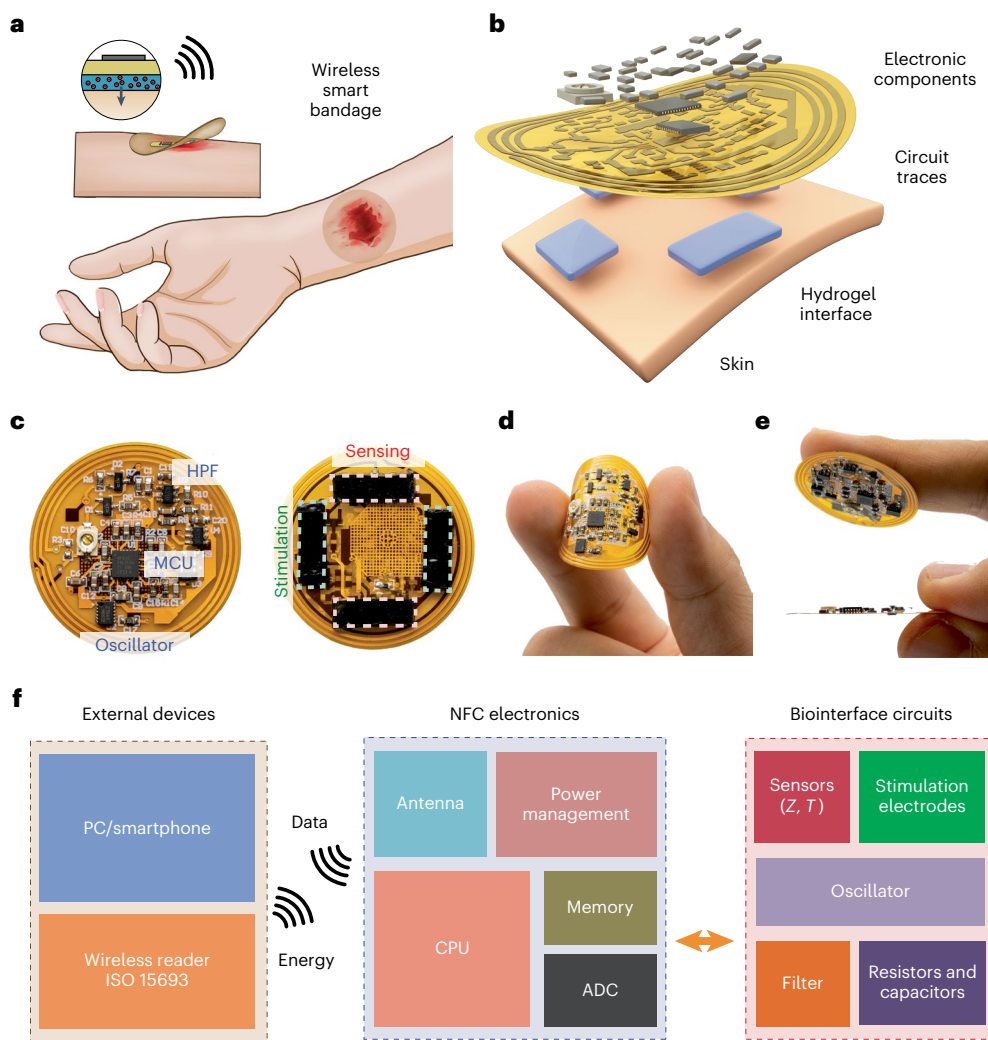


Fig. 1 | Overall design of the wireless smart bandage for chronic wound management. **a,b**, Schematic diagram (**a**) and exploded view (**b**) of the wireless smart bandage including FPCB and tissue-interfacing conducting adhesive hydrogel. **c**, Photographs of the front (left) and back (right) sides of the smart bandage showing the MCU, crystal oscillator, HPF and stimulation and sensing

electrodes. **d,e**, Photographs showing flexibility of the FPCB (**d**) and adhesion of the hydrogel interface and thin layout of the board (**e**, lower). **f**, Block diagram illustrating the key components of the wireless smart bandage system comprising NFC electronics with parallel stimulation and sensing modalities. CPU, central processing unit.

The NFC transponder we used (no. RF430FRL152H) offers two 14-bit analog–digital converters (ADCs) to serve as the analog front-end interface. For optimal monitoring of wound condition, we chose to integrate two sensors (one thermistor and one impedance sensor) that serve as good proxies for determining wound infection and inflammatory states^{15,25,37}. The RF430FRL152H transponder has a direct thermistor support (ADC1 channel) by emitting a small μ A-level current on the thermistor and sampling the voltage. For impedance sensing, an oscillator was used to generate a 32.768-kHz square-wave alternating current (AC) signal (Supplementary Fig. 2) that passed through the wound, and a known impedance component (Z_{known}). Through a voltage divider, the AC signal applied on Z_{known} could then reflect wound impedance (Fig. 2f and Supplementary Fig. 2). This received AC signal was further conditioned through a high-pass filter (HPF) to remove the random direct current (DC) component within the oscillation signal (Fig. 2g and Supplementary Fig. 2). Finally, an envelope detector was used to convert the AC signal amplitude to a DC voltage, which was captured by the ADC0 channel within the RF430FRL152H transponder. With standard impedance components and controlled temperature, we calibrated both ADC channels in our integrated design (Fig. 2h,

and Supplementary Figs. 4 and 5). Finally, the sensing data could be analyzed in real time to provide feedback on the stimulation pattern for closed-loop operation (Supplementary Fig. 6).

Hydrogel interface

To ensure an intimate skin interface and robust electrical communication between the circuit and tissue through the soft hydrogel, the gel electrode interface should have the following characteristics: low contact impedance, high toughness and tunable adhesion. Low contact impedance is required to ensure reliable sensing and efficient charge injection by electrical stimulation. The high toughness requirement is to avoid mechanical damage during motion. Finally, the tissue-interfacing gel needs to have on-demand adhesion to the wound tissue to provide good adhesion during therapy and also easy, gentle removal following external triggers (for example, gentle heating) to mitigate secondary damage to the delicate wounded tissue and prevent a commonly occurring skin condition known as medical adhesive-related skin injury^{38,39} (Fig. 3a).

Here we designed an interpenetrated double-network structure through *in situ* radical polymerization of a thermally responsive

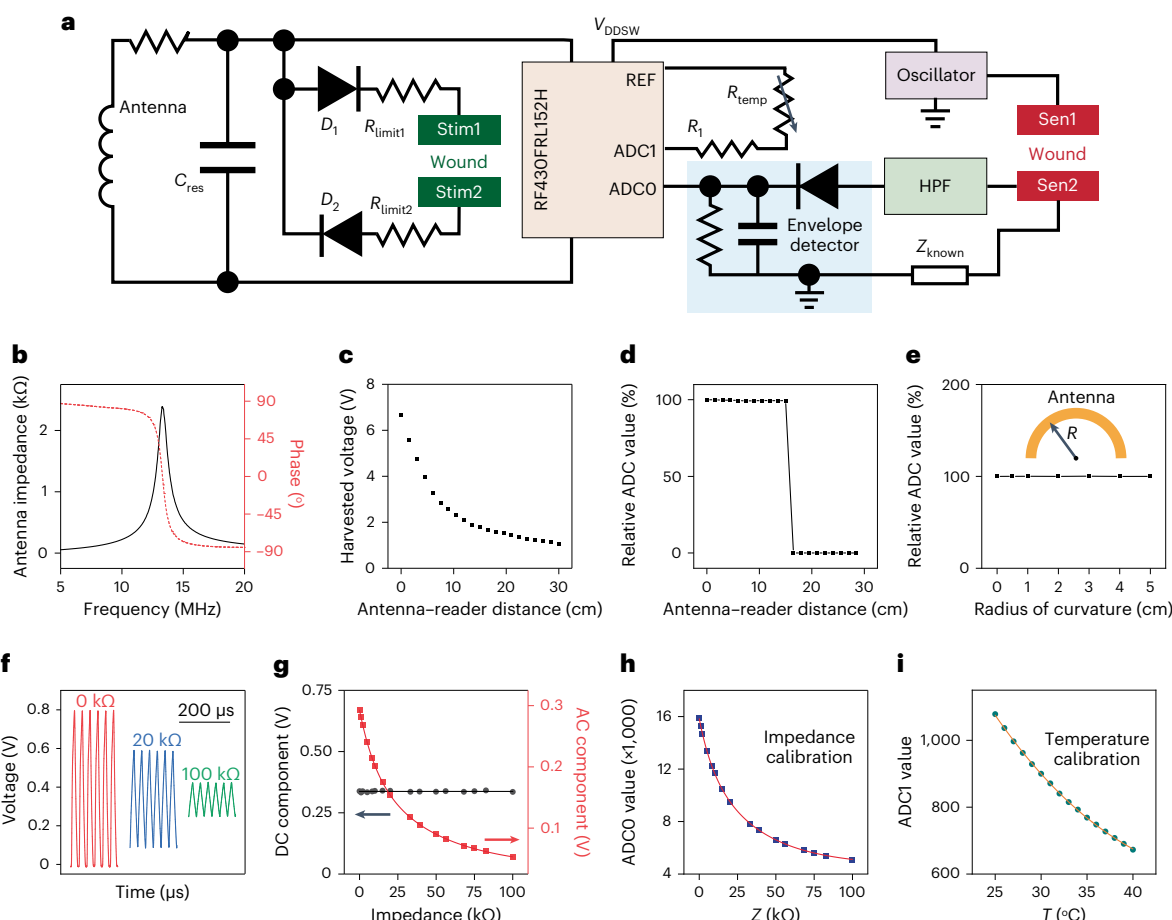


Fig. 2 | Validation of the wireless sensing and stimulation circuits. **a**, Circuit diagram of the wireless smart bandage for simultaneous sensing and stimulation. **b**, Antenna resonant frequency and quality factor as measured by a vector network analyzer (VNA). **c**, Measured RF-harvested voltage as a function of antenna–reader distance. **d**, Wireless readout operation from the microcontroller can function stably up to 15 cm away from the external reader.

e, Wireless sensing can remain stable with bending radius down to 0.5 cm. **f,g**, Voltage output after the HPF showing reduced AC amplitudes with respect to higher resistance values (**f**). Meanwhile, the DC component of the signals remained constant for all resistors tested (**g**). **h,i**, Calibration curves of ADC values under known impedance (**h**) and temperature (**i**).

covalent network of *N*-isopropylacrylamide (NIPAM)⁴⁰ and acrylamide (AAm) in the presence of a physically crosslinked conducting polymer network of PEDOT:PSS (Fig. 3b). Notably, since PEDOT:PSS exists in the form of a colloidal aqueous suspension, it would severely coagulate when mixed with conventional radical initiators that contain both ionic and basic species—that is, ammonium persulfate (AP) and *N,N,N',N'*-tetramethylethylenediamine (TEMED) (Supplementary Fig. 7). To ensure uniform gel formation, we developed a new initiation system based on a nonionic redox pairing of hydrogen peroxide and ascorbic acid that allows for rapid and homogeneous gelation at room temperature (~3 min) (Supplementary Fig. 7).

Compared with the pristine poly(NIPAM-*ran*-AAm) gel, the incorporation of PEDOT:PSS substantially reduced interfacial impedance when in contact with phosphate buffered saline (PBS), with a ~0° phase angle across the entire frequency range (Fig. 3c and Supplementary Fig. 8), corresponding to a resistive nature for the contact due to the high capacitance at the low frequency range for PEDOT:PSS³⁵. Similarly, when a voltage pulse was applied, the PEDOT:PSS gel showed substantially enhanced charge injection capacity when compared with the control sample (Fig. 3d and Supplementary Fig. 9), which ensures efficient delivery of stimulus from the electronically conducting circuits to ionically conducting tissues. The low impedance and high charge injection of the hydrogel electrode can be well maintained

even after 10,000 cycles of repetitive charge injections (Supplementary Fig. 10).

In addition to improved electrical performances, the incorporation of PEDOT:PSS also enhanced the mechanical properties of the hydrogel. Under a unidirectional tensile test, the composite gel can be stretched to a strain similar to that of the control poly-NIPAM gel (~400%) but with a higher Young's modulus, giving rise to enhanced toughness (Fig. 3e and Supplementary Fig. 11). The composite hydrogel is elastic, with reversible impedance changes following stretching to at least 100% strain (Supplementary Fig. 12). Finally, because of the high content of polar moieties in the NIPAM-AAm backbone, the composite hydrogel can have polar interactions in addition to van der Waals interactions with diverse surfaces including plastic, metal, rubber or skin, to provide its strong interfacial adhesion (Fig. 3f and Supplementary Figs. 13 and 14).

Although hydrogels containing NIPAM and PEDOT:PSS have previously been studied⁴¹, a dual-conducting hydrogel with on-demand tissue adhesion and detachment has not been reported. Poly-NIPAM is a well-known polymer that exhibits a lower critical solution temperature (LCST) in water due to heat-induced aggregation of the amphiphilic NIPAM units⁴⁰. In our case, we observed that LCST transition was associated with marked changes in gel adhesion, probably because the aggregated backbones can no longer form effective bonding sites

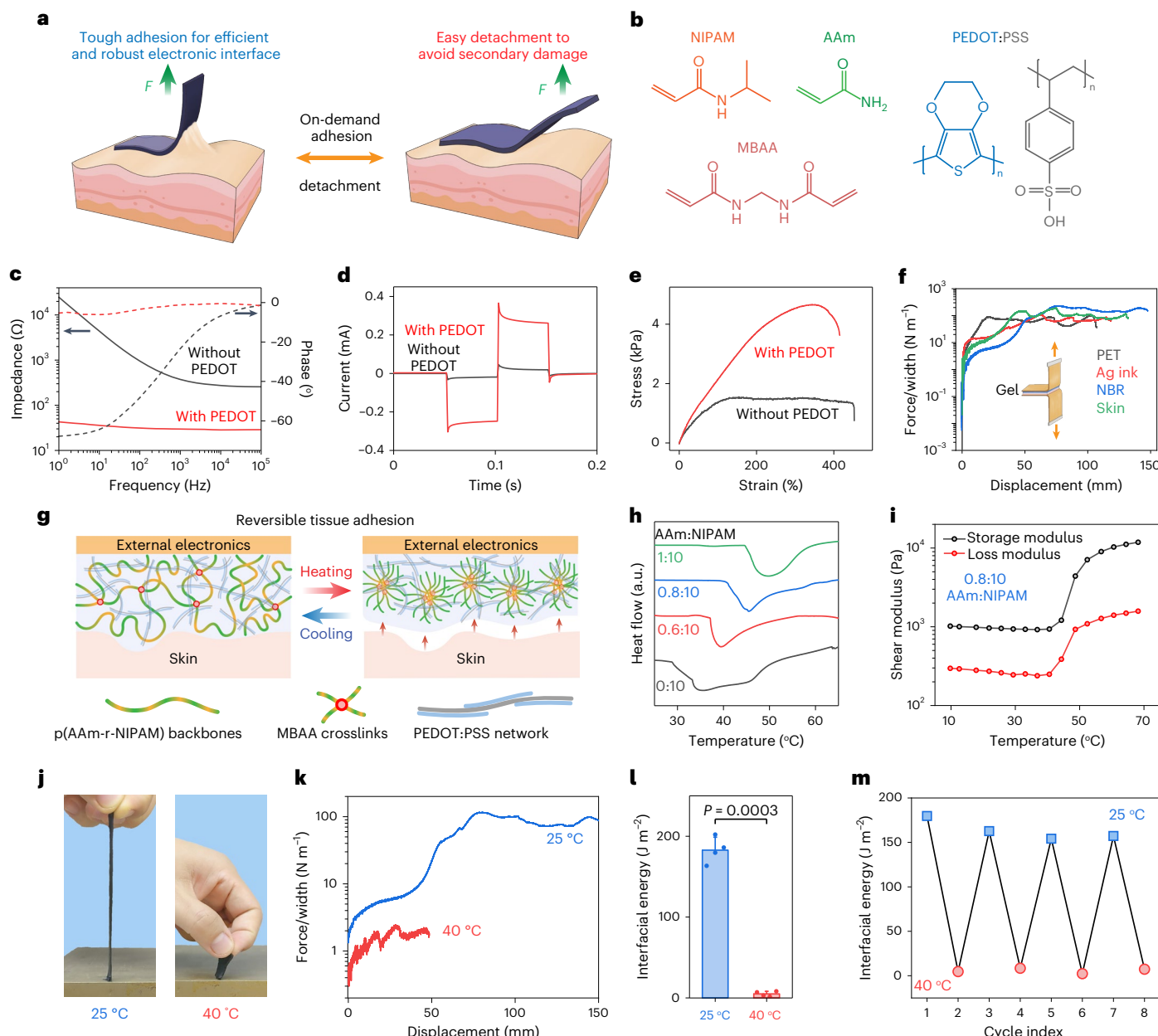


Fig. 3 | Tough and low-impedance conductive hydrogel electrode with on-demand tissue adhesion and detachment. **a**, Schematic diagram illustrating the requirements for the hydrogel interface in the smart bandage. During device operation, the hydrogel electrode must possess simultaneously high toughness and adhesion to avoid damage or detachment. When peeling off the device after the treatment period, the tissue-interfacing gel must be easily detachable to minimize secondary damage to the delicate wounded tissue. **b**, Molecular structures of the monomers, crosslinker and conducting polymer for the interpenetrated double network. **c,d**, Electrochemical impedance spectroscopy (EIS) (**c**) and chronoamperometry (**d**) of hydrogels with (20 mg ml⁻¹ PEDOT:PSS with 150 mg ml⁻¹ NIPAM and 12 mg ml⁻¹ AAm) and without (150 mg ml⁻¹ NIPAM and 12 mg ml⁻¹ AAm only) PEDOT:PSS. **e**, Unidirectional tensile testing of hydrogels with and without PEDOT:PSS. **f**, 180° peeling test of the conducting hydrogel on various surfaces including polyethylene terephthalate (PET), screen-printed

and dried silver (Ag) ink, nitrile butadiene rubber (NBR) and mouse skin tissue. **g**, Schematic diagram illustrating microscopic structural changes during LCST phase transition. **h**, DSC scans of the hydrogel interface with different weight ratios of AAm to NIPAM. The hydrogel consists of 150 mg ml⁻¹ NIPAM, 20 mg ml⁻¹ PEDOT:PSS and AAm of 0, 9, 12 and 15 mg ml⁻¹. **i**, Rheological measurement showing phase transition temperature of the sample when the AAm:NIPAM weight ratio is 0.8:10. **j–l**, Photographs (**j**) and 180° peeling test (**k**) showing marked differences (**l**) in adhesion for the gel at room temperature and 40 °C. $n = 4$ for both conditions. All data presented as mean \pm s.d. Two-tailed *t*-testing assuming equal variances was performed for *P* values. **m**, The tunable hydrogel adhesion can be cycled multiple times due to the reversible nature of the LCST phenomenon. **j–m**, The hydrogel consists of 150 mg ml⁻¹ NIPAM, 12 mg ml⁻¹ AAm and 20 mg ml⁻¹ PEDOT:PSS. a.u., arbitrary units.

with external surfaces (Fig. 3g). We found that additional hydrophilic monomers of AAm can be used to tune the LCST point to higher levels (that is, above body temperature)⁴², as indicated by differential scanning calorimetry (DSC) (Fig. 3h). When the mass ratio between AAm and NIPAM monomers was 0.8:10, the phase change temperature

reached -40 °C, as confirmed by both DSC and rheological measurements (Fig. 3h,i). When tested on metal and mouse skin, the hydrogel electrodes showed strong adhesion at room temperature or normal skin temperature, comparable to 3M Kind Removal Silicone Tape used to secure gauze to the skin, but completely lost its adhesion with two

orders of magnitude lower interfacial energy when heated $>40\text{ }^{\circ}\text{C}$ (Fig. 3j–l and Supplementary Figs. 15 and 16). Of note, phase transition will not occur gradually before the critical temperature, as evidenced by DSC and rheology (Fig. 3h,j), which prevents undesired detachment during normal operation (Supplementary Fig. 17). Finally, because the LCST process is reversible⁴³, the tunable adhesion of the same hydrogel can be repeated multiple times with minimal degradation of low-temperature adhesion (Fig. 3m).

Validation in preclinical wound models

To validate our wound care management system, we performed a series of preclinical evaluations to test the robustness and efficacy of our developed device in its ability to monitor wound conditions and deliver timely treatment. We first confirmed that mice wearing our wireless devices were able to move freely, with a distance traveled similar to that of mice with no device attached, demonstrating an ideal therapeutic modality for patient use: namely, lightweight and untethered with cables (Fig. 4a,b). More importantly, our temperature and impedance sensors were able to monitor wound state continuously as the mice moved freely in the cage (Fig. 4c and Supplementary Fig. 18). In addition, our hydrogel was biocompatible and did not initiate any sensitization or irritation after continuous contact with the skin over 15 days, demonstrating absence of adverse reactivity signs compared with normal skin (Supplementary Fig. 19 and Supplementary Table 2).

To test the functionality of our platform in a biological system, a splinted excisional wound mouse model was used in which stimulated mice were treated with continuous electrical pulses. Control mice received standard sterile wound dressings without electrical stimulation. We found that stimulation resulted in accelerated wound closure (Fig. 4d,e) and a significant increase in wound impedance to attain a faster impedance plateau, signifying a return to an unwounded state^{15,25} (Fig. 4f and Supplementary Fig. 20). Stimulation of wounds also improved functional tensile recovery with increased dermal thickness, collagen deposition and overall dermal appendage count (Fig. 4g,h and Supplementary Figs. 21–23). Of note, compared with a wired modality, our smart bandage allowed for longer and potentially continuous treatment durations (Supplementary Fig. 22), which have been linked to accelerated wound closure³¹. Stimulated wounds also showed an increase in collagen fiber heterogeneity, resulting in more random, shorter and less aligned fiber orientations (Supplementary Figs. 24 and 25).

We further observed a significant increase in neovascularization among stimulated wounds, with increased microvessel count and higher expression of CD31 and α -smooth muscle actin (α -SMA) (Fig. 4h–j and Supplementary Fig. 26). Similar results were also observed in a murine burn wound-healing model (Supplementary Figs. 27–30). Our smart bandage was also found to significantly reduce infection in the wound, decreasing overall bacterial colony count (Fig. 4k,l). Moreover, by continuous monitoring of wound impedance and temperature, our wireless smart bandage could detect early onset of infection and modulate treatment in a closed-loop manner to avoid further wound complications (Supplementary Fig. 31). In current clinical practice, doctors still rely on qualitative markers such as swelling or erythema (that is, superficial reddening of the skin) to identify wound infections, which are often difficult to judge in the early stages of biofilm development. With quantitative biophysical signals recorded by our smart bandage, we can provide treatment when clinically used markers are still ambiguous, enabling timely treatment of chronic wounds, reduction in hospital readmissions and medical cost and improvement in patient wound-healing outcomes⁴⁴. We further validated our system in a streptozotocin (STZ)-induced diabetic excisional wound model⁴⁵, also observing an accelerated time to wound closure, improved dermal collagen fiber heterogeneity and increased vascularization (Supplementary Figs. 32–35). An STZ model most closely resembles type I diabetes in patients⁴⁶. On the cellular level, we observed the expected

ability of our device to prompt cell alignment and migration, inducible with a directional electric field (Supplementary Figs. 36 and 37).

Cellular and molecular mechanisms

Although the beneficial effects of electrical stimulation have previously been reported³², the cellular and molecular mechanisms for this effect remain obscure. Previous works have evaluated the role of electrical stimulation in enhancing wound healing through the activation of fibroblasts and keratinocytes, both known major cell types of the dermis that are active in the inflammatory phase of cutaneous wound repair^{47–51}. Inflammatory signals activate the maturation and crosstalk between these two cell types, coordinating the migration and restoration of normal tissue homeostasis after wounding^{52,53}. However, the effect of electrical stimulation on immune cells, namely circulating cells, which are critical regulators of all stages of wound healing from early inflammation until late fibrosis^{54,55}, remains unexplored.

In our work, due to the lightweight and untethered features of our smart bandage, we were able to evaluate the long-term effects of electrical stimulation on circulating cells involved in wound repair using a complex parabiosis model⁵⁶. This would not have been possible previously because, with a conventional wired modality, parabiosis under a long anesthesia regimen would not survive. To execute this, we performed parabiosis of five green fluorescence protein (GFP)-positive mice to wild-type (WT) mice. WT mice were wounded and either subjected to electrical stimulation or left untreated. Wound tissues from both groups were explanted on day 5 and their transcriptional profiles analyzed by single-cell RNA sequencing (scRNA-seq) using the 10X Genomics Chromium platform (Fig. 5a). Of all the circulating inflammatory cells activated by our smart bandage (Fig. 5b and Supplementary Fig. 38), monocytes and macrophages had the highest number of differentially expressed genes in both electrically stimulated and untreated wounds (Fig. 5c,d and Supplementary Fig. 39). Even with many neutrophils present, the magnitude of differentially expressed genes did not reach statistical significance (Supplementary Figs. 38 and 39). Similarly, while there were higher numbers of B and T cells in the stimulated group, signifying greater recruitment of these cells from the circulation^{57,58}, the overall number of cells was low and the amount of differentially expressed genes was nominal (Supplementary Figs. 38 and 39).

To specifically investigate macrophages and monocytes, we performed a series of evaluations to validate and define the high number of differentially expressed genes observed. First, we re-embedded our macrophages and monocytes and used cellular trajectory reconstruction analysis using gene counts and expression (CytoTRACE) to confirm that our defined monocytes possessed less differentiated cell states based on the distribution of unique messenger RNA transcripts (Fig. 5e). We then overlaid the stimulated and unstimulated macrophages and monocytes and performed RNA velocity and pseudotime analyses using scVelo and Monocle 3, respectively, to combine RNA velocity information with trajectory inference to compute a map of potential fates that the macrophages and monocytes can undergo in response to electrical stimulation. We first used scVelo to infer our root node and transcriptional directionality across the manifold, based on mRNA splicing of macrophages and monocytes. We found three general transcriptional vector paths in which mRNA splicing could occur within individual cells, with a relatively higher amount of differentiated individual cells found on the left of the embedding and less differentiated cells on the right (Supplementary Fig. 40a), further confirming CytoTRACE. We then performed pseudotime analysis with Monocle 3, using a root node identified with scVelo (marked with a circle in the right-hand panel of Fig. 5e) to infer terminal cell states⁵⁹. Our analysis once again revealed three distinct transcriptional trajectories, with stimulated cells clustered mainly along trajectories 1 (right) and 2 (middle), while trajectory 3 (left) was mainly composed of unstimulated cells (Fig. 5e and Supplementary Fig. 40b).

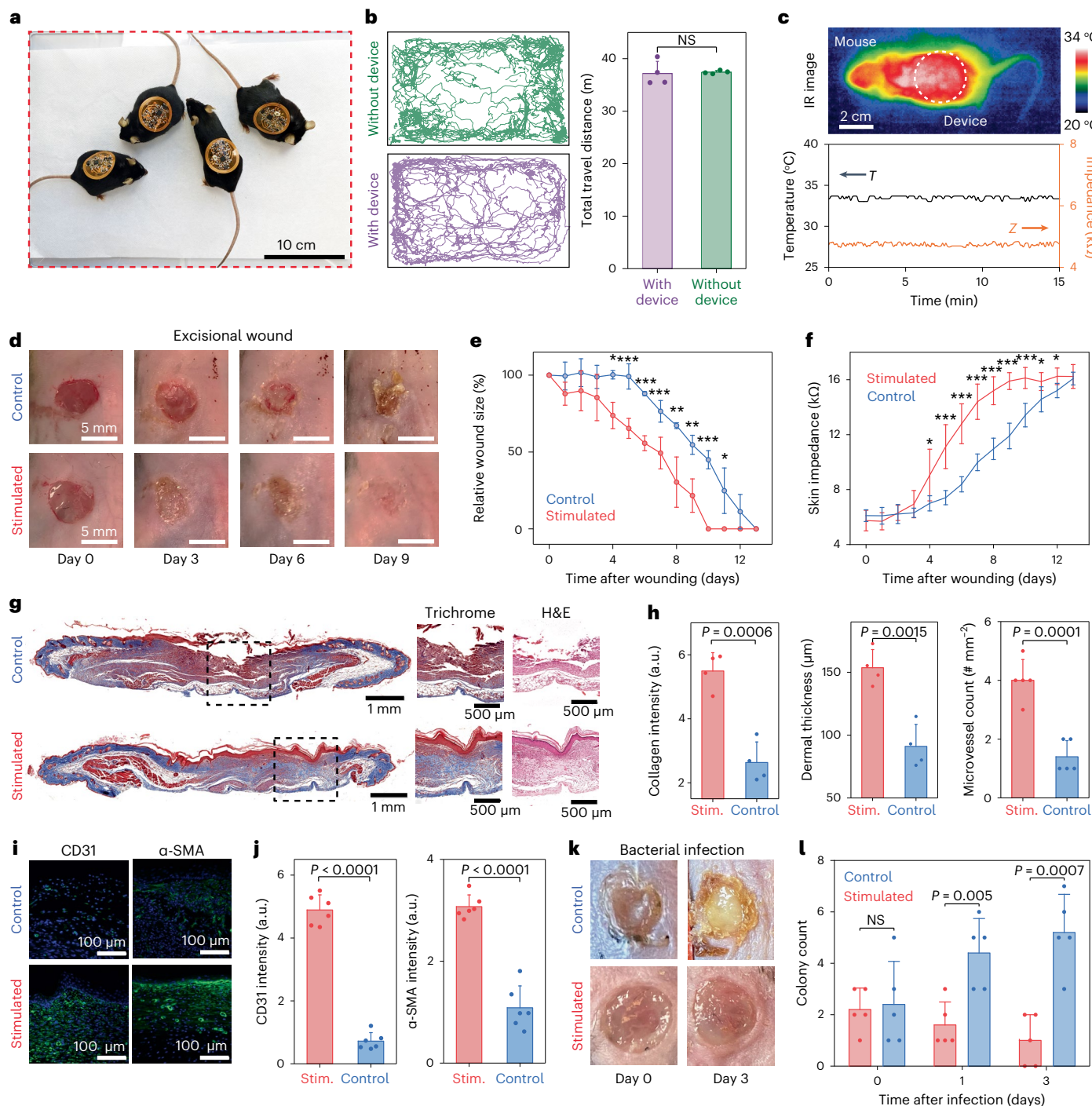


Fig. 4 | Wireless smart bandage can continuously monitor wound physiological conditions and accelerate tissue regeneration. a, Photograph of freely moving mice wearing wireless smart bandages. **b**, Representative trajectories of mice with and without the smart bandage in the open-field test (left), and statistical analysis between two groups (right). Four mice in each group were used in the test. **c**, IR image of a mouse wearing the smart bandage (top) and raw traces of wirelessly sensed temperature and impedance (bottom). **d**, Representative photographs showing the progression of wound regeneration in an excisional wound healing model with and without electrical stimulation treatment. **e,f**, Relative size (e) and impedance (f) of excisional wounds over time, indicating accelerated tissue regeneration with stimulation. $n = 5$ for each group. All data presented as mean \pm s.d. Two-tailed *t*-testing assuming equal variances was performed. For wound size, day 4 (D4) $P = 0.05$, D5 $P = 0.001$, D6 $P = 0.001$, D7 $P = 0.001$, D8 $P = 0.01$, D9 $P = 0.01$, D10 $P = 0.001$, D11 $P = 0.05$. For impedance, D4 $P = 0.04$, D5 $P = 0.001$, D6 $P = 0.0002$, D7 $P = 0.0001$, D8 $P = 0.00007$, D9 $P = 0.00004$, D10 $P = 0.0007$, D11 $P = 0.03$, D12 $P = 0.02$. ${}^{***}P < 0.001$, ${}^{**}P < 0.01$, ${}^*P < 0.05$.

${}^{***}P < 0.001$. **g**, Representative cross-sectional histologic images of skin tissue harvested from mice with and without stimulation after 13 days. Left and middle, Masson's trichrome; right, hematoxylin and eosin (H&E). Black dashed boxes denote the area for zoomed-in views in the middle and right panels highlighting healed tissue. **h**, Quantitative comparison of collagen intensity, dermal thickness and microvessel count for skin tissue with and without stimulation. All data presented as mean \pm s.d. Two-tailed *t*-testing assuming equal variances was performed. $n = 4$ for each sample. **i,j**, Immunostaining images (i) and quantitative comparison (j) of CD31 and α -SMA from tissue with and without stimulation. All data presented as mean \pm s.d. Two-tailed *t*-testing assuming equal variances was performed. $n = 6$ for each sample. $P = 4.4 \times 10^{-9}$ for CD31, $P = 1.6 \times 10^{-6}$ for α -SMA. **k,l**, Representative photographs (k) and quantitative comparison (l) of wounds infected with *E. coli*, with and without stimulation. All data presented as mean \pm s.d. Two-tailed *t*-testing assuming equal variances was performed. NS, not significant.

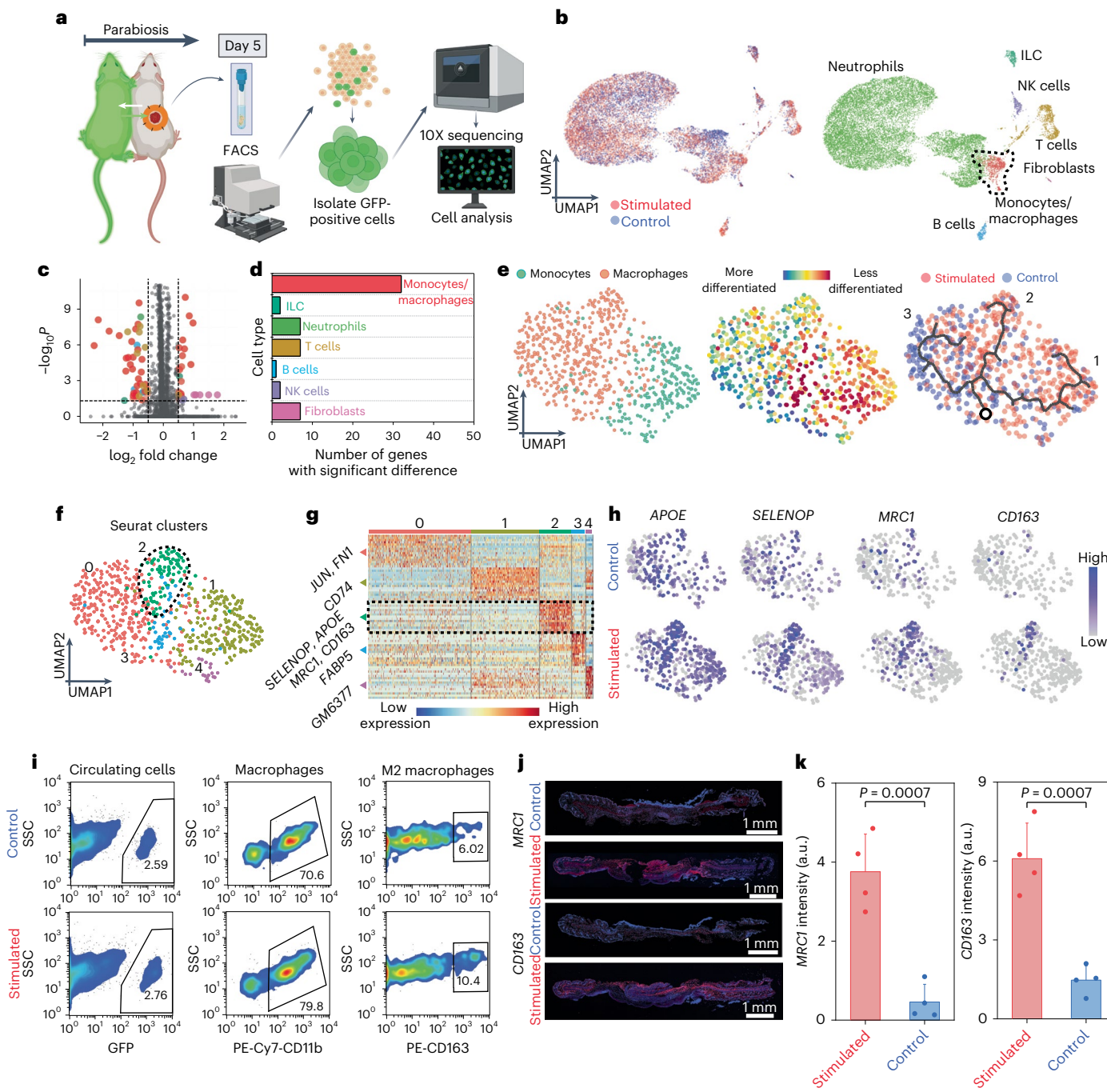


Fig. 5 | Molecular mechanism involved in accelerated tissue regeneration with electrical stimulation. **a**, Schematic diagram illustrating the experimental flow for scRNA-seq. Tissues from an excisional wound of a WT mouse paired with a GFP-positive mouse, subjected to either treatment (that is, stimulation) or not (that is, control), were sorted for GFP-positive cells using FACS and analyzed by 10X sequencing. Illustration created with BioRender.com. **b**, UMAP embedding of all cells colored by cell type suggesting equal overlap of stimulated and control cells. **c,d**, Number of differentially expressed genes (**c**, \log_2 fold change > 0.5 and $P < 0.05$) for all cell types (**d**). Two-tailed *t*-testing assuming equal variances was performed for *P* values. **e**, UMAP embedding, split by macrophages and monocytes (left), verified with the CytoTrace platform (middle), which identifies differentiated cell states within the monocyte cluster. RNA velocity (right), shown as the main gene-averaged flow, visualized by velocity streamlines projected onto UMAP embedding of the monocyte cluster categorized by treatment group. **f**, UMAP embedding of macrophage and monocyte Seurat clusters grouped

by cells of similar differential expression, with proregenerative cluster 2, outlined by the dotted black circle, showing that there are five transcriptionally distinct clusters. **g**, Heatmap of the top differentially expressed genes in each Seurat cluster. **h**, Feature plots, split by treatment (stimulated) and control, of differentially expressed genes upregulated in cluster 2 in macrophages and monocytes, indicate that there is enrichment for proregenerative markers localized around cluster 2 and trajectory 2, consisting primarily of stimulated macrophages. **i**, FACS plots for treatment and control groups of GFP-positive cells circulating in the parabiosis wound model verify a higher percentage of M2 macrophages in the stimulated group. **j,k**, Images (**j**) and quantitative comparison (**k**) of *MRC1* and *CD163* from tissue with and without stimulation verifying M2 macrophage markers. $n = 4$ for each sample. All data presented as mean \pm s.d. Two-tailed *t*-testing assuming equal variances was performed for *P* values. SSC, side scattering; ILC, innate lymphoid cell; NK, natural killer cell.

To further understand why macrophages and monocytes had a higher amount of differentially expressed genes activated by our smart bandage, we performed uniform manifold approximation and projection (UMAP)-based clustering, which revealed five transcriptionally distinct clusters (Fig. 5f and Supplementary Fig. 41). Of the five clusters, cluster 0, consisting of both macrophages and unstimulated control cells, had a higher expression of genes such as *JUN* and *FNI* (refs. ^{60,61}), which have previously been associated with wound healing, whereas clusters 1, 2 and 3, consisting predominantly of stimulated monocytes and macrophages, demonstrated elevated expression of genes involved in the wound repair process, such as *CD74*, *SELENOP*, *APOE*, *MRC1*, *CD163* and *FABP5* (refs. ^{62–65}) (Fig. 5g).

Interestingly, when we looked at the stimulated and control feature plots of highly expressed genes in macrophages and monocytes, we saw that cells with a strong enrichment for previously reported proregenerative markers, notably *CD163* and *MRC1* (CD206), as well as *SELENOP* and *APOE*, all localized around Seurat cluster 2 and trajectory 2 (middle), which primarily contained stimulated macrophages (Fig. 5h and Supplementary Fig. 42). *CD163* and *MRC1* (CD206) have previously been described as M2 anti-inflammatory macrophage markers⁶⁶ while *SELENOP* has been found to be anti-inflammatory, regulating macrophage invasiveness and other inflammatory mediators responsible for pathogen clearance and tissue repair, and is linked to M2 macrophage markers such as *STAB1*, *SEPP1* and *ARG1* (ref. ⁶³). *APOE* has been also shown to enhance *in vitro* phagocytosis of macrophages, increasing muscle and soft tissue regeneration^{67,68}.

We further confirmed these transcriptional changes at the protein level, performing flow cytometry on GFP-positive cells circulating to wounds in our parabiosis model. We identified a higher percentage of *CD163*-positive cells in stimulated wounds as compared with controls (Fig. 5i and Supplementary Fig. 43). This was further confirmed by immunofluorescent staining of healed tissue, with significantly higher *CD163* and *CD206* expression observed in stimulated as compared with untreated wounds (Fig. 5j,k).

These data suggest that electrical stimulation may drive macrophages towards a more regenerative phenotype, and could underly the accelerated wound healing observed in our preclinical studies. The high predominance of regenerative macrophages could, in part, be due to macrophages responding to local microenvironmental stimuli. Modulation of the cell membrane electric potential with electrical stimuli could activate more ATP-sensitive potassium ion channels, which has previously been shown to affect macrophage differentiation plasticity and function^{69,70}. Taken together, our pre-clinical studies attribute one mechanism by which electrical stimulation may coordinate and regulate macrophage functions, including those essential for microbial clearance and wound healing. Our smart bandage, in turn, will enable further biological discovery and allow for researchers to explore hypotheses previously less well studied due to current treatment modality limitations and animal model complexities.

Conclusions

In summary, we designed and fabricated a miniaturized smart bandage with dual-channel continuous sensing of wound impedance and temperature, as well as a parallel stimulation circuit to deliver programmed electrical cues for accelerated wound healing. Through the integration of sensors and stimulators into one wearable patch, as well as rational design of tissue-interfacing hydrogel electrodes, our wireless smart bandage enables (1) active monitoring and closed-loop treatment of a wound and (2) accelerated healing through a proregenerative mode of action, activated by increased cellular proliferation and recruitment of cells involved in wound repair. This dual-mode integration advances the field of wound healing pathobiology, enabling the optimization of treatment modalities that would allow for better patient mobility and improvement in standard of care.

However, additional challenges exist, including production scalability (for example, reduced cost, long-term storage), incorporation of additional sensors (for example, metabolites, biomarkers, pH) and clinical translatability (for example, biocompatibility, biofouling issues). While our preclinical demonstrations showed proof of concept, future work involves extending our smart bandage to a human-sized form factor and running preliminary tests in large-animal models followed by human trials. In addition, we aim to reduce the manufacturing cost of our clinical device to enable broad adoption within a payer system. Finally, our device platform may also be adapted to the management of other diseases, enabling the next generation of closed-loop bioelectronic medicine.

Online content

Any methods, additional references, Nature Research reporting summaries, source data, extended data, supplementary information, acknowledgements, peer review information; details of author contributions and competing interests; and statements of data and code availability are available at <https://doi.org/10.1038/s41587-022-01528-3>.

References

1. Han, G. & Ceilley, R. Chronic wound healing: a review of current management and treatments. *Adv. Ther.* **34**, 599–610 (2017).
2. Werdin, F., Tenenhaus, M. & Rennekampff, H.-O. Chronic wound care. *Lancet* **372**, 1860–1862 (2008).
3. Gurtner, G. C., Werner, S., Barrandon, Y. & Longaker, M. T. Wound repair and regeneration. *Nature* **453**, 314–321 (2008).
4. Martin, P. Wound healing—aiming for perfect skin regeneration. *Science* **276**, 75–81 (1997).
5. Singer, A. J. & Clark, R. A. Cutaneous wound healing. *N. Engl. J. Med.* **341**, 738–746 (1999).
6. Frykberg, R. G. & Banks, J. Challenges in the treatment of chronic wounds. *Adv. Wound Care* **4**, 560–582 (2015).
7. Rodrigues, M., Kosaric, N., Bonham, C. A. & Gurtner, G. C. Wound healing: a cellular perspective. *Physiol. Rev.* **99**, 665–706 (2019).
8. McLister, A., McHugh, J., Cundell, J. & Davis, J. New developments in smart bandage technologies for wound diagnostics. *Adv. Mater.* **28**, 5732–5737 (2016).
9. Derakhshandeh, H., Kashaf, S. S., Aghabaglou, F., Ghanavati, I. O. & Tamayol, A. Smart bandages: the future of wound care. *Trends Biotechnol.* **36**, 1259–1274 (2018).
10. Long, Y. et al. Effective wound healing enabled by discrete alternative electric fields from wearable nanogenerators. *ACS Nano* **12**, 12533–12540 (2018).
11. Liu, A. et al. Accelerated complete human skin architecture restoration after wounding by nanogenerator-driven electrostimulation. *J. Nanobiotechnol.* **19**, 280 (2021).
12. Farahani, M. & Shafee, A. Wound healing: from passive to smart dressings. *Adv. Healthc. Mater.* **10**, e2100477 (2021).
13. Dincer, C. et al. Disposable sensors in diagnostics, food, and environmental monitoring. *Adv. Mater.* **31**, e1806739 (2019).
14. Barros Almeida, I. et al. Smart dressings for wound healing: a review. *Adv. Skin Wound Care* **34**, 1–8 (2021).
15. Kekonen, A. et al. Bioimpedance sensor array for long-term monitoring of wound healing from beneath the primary dressings and controlled formation of H_2O_2 using low-intensity direct current. *Sensors* **19**, 2505 (2019).
16. Lukaski, H. C. & Moore, M. Bioelectrical impedance assessment of wound healing. *J. Diabetes Sci. Technol.* **6**, 209–212 (2012).
17. Chanmugam, A. et al. Relative temperature maximum in wound infection and inflammation as compared with a control subject using long-wave infrared thermography. *Adv. Skin Wound Care* **30**, 406–414 (2017).
18. Tamayol, A. et al. Flexible pH-sensing hydrogel fibers for epidermal applications. *Adv. Healthc. Mater.* **5**, 711–719 (2016).

19. Xu, G. et al. Battery-free and wireless smart wound dressing for wound infection monitoring and electrically controlled on-demand drug delivery. *Adv. Funct. Mater.* **31**, 2100852 (2021).
20. Trung, T. Q., Ramasundaram, S., Hwang, B. U. & Lee, N. E. An all-elastomeric transparent and stretchable temperature sensor for body-attachable wearable electronics. *Adv. Mater.* **28**, 502–509 (2016).
21. Hattori, Y. et al. Multifunctional skin-like electronics for quantitative, clinical monitoring of cutaneous wound healing. *Adv. Healthc. Mater.* **3**, 1597–1607 (2014).
22. Shi, X. & Wu, P. A smart patch with on-demand detachable adhesion for bioelectronics. *Small* **17**, e2101220 (2021).
23. Pang, Q. et al. Smart flexible electronics-integrated wound dressing for real-time monitoring and on-demand treatment of infected wounds. *Adv. Sci.* **7**, 1902673 (2020).
24. Marks, H. et al. A paintable phosphorescent bandage for postoperative tissue oxygen assessment in DIEP flap reconstruction. *Sci. Adv.* **6**, eabd1061 (2020).
25. Swisher, S. L. et al. Impedance sensing device enables early detection of pressure ulcers *in vivo*. *Nat. Commun.* **6**, 6575 (2015).
26. McCaffrey, C., Flak, J., Kiri, K. & Pursula, P. Flexible bioimpedance spectroscopy system for wound care monitoring. In *2019 IEEE Biomedical Circuits and Systems Conference (BioCAS)* 1–4 (IEEE, 2019).
27. Kalidasan, V. et al. Wirelessly operated bioelectronic sutures for the monitoring of deep surgical wounds. *Nat. Biomed. Eng.* **5**, 1217–1227 (2021).
28. Zhao, Y. et al. Skin-Inspired antibacterial conductive hydrogels for epidermal sensors and diabetic foot wound dressings. *Adv. Funct. Mater.* **29**, 1901474 (2019).
29. Ciani, I. et al. Development of immunosensors for direct detection of three wound infection biomarkers at point of care using electrochemical impedance spectroscopy. *Biosens. Bioelectron.* **31**, 413–418 (2012).
30. Gao, Y. et al. A flexible multiplexed immunosensor for point-of-care *in situ* wound monitoring. *Sci. Adv.* **7**, eabg9614 (2021).
31. Thakral, G. et al. Electrical stimulation to accelerate wound healing. *Diabet. Foot Ankle* **4**, 22081 (2013).
32. Kloth, L. C. Electrical stimulation technologies for wound healing. *Adv. Wound Care* **3**, 81–90 (2014).
33. Zhao, M. et al. Electrical signals control wound healing through phosphatidylinositol-3-OH kinase-gamma and PTEN. *Nature* **442**, 457–460 (2006).
34. Cohen, D. J., Nelson, W. J. & Maharbiz, M. M. Galvanotactic control of collective cell migration in epithelial monolayers. *Nat. Mater.* **13**, 409–417 (2014).
35. Liu, Y. et al. Soft and elastic hydrogel-based microelectronics for localized low-voltage neuromodulation. *Nat. Biomed. Eng.* **3**, 58–68 (2019).
36. Jiang, Y. et al. Topological supramolecular network enabled high-conductivity, stretchable organic bioelectronics. *Science* **375**, 1411–1417 (2022).
37. Power, G., Moore, Z. & O'Connor, T. Measurement of pH, exudate composition and temperature in wound healing: a systematic review. *J. Wound Care* **26**, 381–397 (2017).
38. Kelly-O'Flynn, S., Mohamud, L. & Copson, D. Medical adhesive-related skin injury. *Br. J. Nurs.* **29**, S20–S26 (2020).
39. Fumarola, S. et al. Overlooked and underestimated: medical adhesive-related skin injuries. *J. Wound Care* **29**, S1–S24 (2020).
40. Schild, H. G. Poly(N-isopropylacrylamide): experiment, theory and application. *Prog. Polym. Sci.* **17**, 163–249 (1992).
41. Cao, S., Tong, X., Dai, K. & Xu, Q. A super-stretchable and tough functionalized boron nitride/PEDOT:PSS/poly(Nisopropylacrylamide)hydrogel with self-healing, adhesion, conductive and photothermal activity. *J. Mater. Chem. A* **7**, 8204–8209 (2019).
42. Fundueanu, G., Constantin, M. & Ascenzi, P. Poly(y(N-isopropylacrylamide-co-acrylamide) cross-linked thermoresponsive microspheres obtained from preformed polymers: influence of the physico-chemical characteristics of drugs on their release profiles. *Acta Biomater.* **5**, 363–373 (2009).
43. Zhang, Q., Weber, C., Schubert, U. S. & Hoogenboom, R. Thermoresponsive polymers with lower critical solution temperature: from fundamental aspects and measuring techniques to recommended turbidimetry conditions. *Mater. Horiz.* **4**, 109–116 (2017).
44. Negut, I., Grumezescu, V. & Grumezescu, A. M. Treatment strategies for infected wounds. *Molecules* **23**, 2392 (2018).
45. Chen, H. et al. Dissolved oxygen from microalgae-gel patch promotes chronic wound healing in diabetes. *Sci. Adv.* **6**, eaba4311 (2020).
46. Wu, J. & Yan, L. J. Streptozotocin-induced type 1 diabetes in rodents as a model for studying mitochondrial mechanisms of diabetic β cell glucotoxicity. *Diabetes Metab. Syndr. Obes.* **8**, 181–188 (2015).
47. Schutzius, G. et al. BET bromodomain inhibitors regulate keratinocyte plasticity. *Nat. Chem. Biol.* **17**, 280–290 (2021).
48. Mahmoudi, S. et al. Heterogeneity in old fibroblasts is linked to variability in reprogramming and wound healing. *Nature* **574**, 553–558 (2019).
49. Chen, K. et al. Disrupting biological sensors of force promotes tissue regeneration in large organisms. *Nat. Commun.* **12**, 5256 (2021).
50. Trotsuk, A. A. et al. Inhibiting fibroblast mechanotransduction modulates severity of idiopathic pulmonary fibrosis. *Adv. Wound Care* **11**, 511–523 (2022).
51. Barrera, J. A. et al. Adipose-derived stromal cells seeded in pullulan-collagen hydrogels improve healing in murine burns. *Tissue Eng. Part A* **27**, 844–856 (2021).
52. Barrientos, S., Stojadinovic, O., Golinko, M. S., Brem, H. & Tomic-Canic, M. Growth factors and cytokines in wound healing. *Wound Repair Regen.* **16**, 585–601 (2008).
53. Chen, K. et al. Mechanical strain drives myeloid cell differentiation toward proinflammatory subpopulations. *Adv. Wound Care* **11**, 466–478 (2022).
54. Kim, S. Y. & Nair, M. G. Macrophages in wound healing: activation and plasticity. *Immunol. Cell Biol.* **97**, 258–267 (2019).
55. Wynn, T. A. & Vannella, K. M. Macrophages in tissue repair, regeneration, and fibrosis. *Immunity* **44**, 450–462 (2016).
56. Duyverman, A. M., Kohno, M., Duda, D. G., Jain, R. K. & Fukumura, D. A transient parabiosis skin transplantation model in mice. *Nat. Protoc.* **7**, 763–770 (2012).
57. Sirbulescu, R. F. et al. Mature B cells accelerate wound healing after acute and chronic diabetic skin lesions. *Wound Repair Regen.* **25**, 774–791 (2017).
58. Hofmann, U. et al. Activation of CD4 $^{+}$ T lymphocytes improves wound healing and survival after experimental myocardial infarction in mice. *Circulation* **125**, 1652–1663 (2012).
59. Bergen, V., Lange, M., Peidli, S., Wolf, F. A. & Theis, F. J. Generalizing RNA velocity to transient cell states through dynamical modeling. *Nat. Biotechnol.* **38**, 1408–1414 (2020).
60. Wernig, G. et al. Unifying mechanism for different fibrotic diseases. *Proc. Natl Acad. Sci. USA* **114**, 4757–4762 (2017).
61. Wang, J. et al. High expression of Fibronectin 1 suppresses apoptosis through the NF- κ B pathway and is associated with migration in nasopharyngeal carcinoma. *Am. J. Transl. Res.* **9**, 4502–4511 (2017).

62. Farr, L., Ghosh, S. & Moonah, S. Role of MIF cytokine/CD74 receptor pathway in protecting against injury and promoting repair. *Front. Immunol.* **11**, 1273 (2020).
63. Carlson, B. A. et al. Selenoproteins regulate macrophage invasiveness and extracellular matrix-related gene expression. *BMC Immunol.* **10**, 57 (2009).
64. Lin, J. D. et al. Single-cell analysis of fate-mapped macrophages reveals heterogeneity, including stem-like properties, during atherosclerosis progression and regression. *JCI Insight* **4**, e124574 (2019).
65. Huang, Z. H., Reardon, C. A. & Mazzone, T. Endogenous ApoE expression modulates adipocyte triglyceride content and turnover. *Diabetes* **55**, 3394–3402 (2006).
66. Martinez, F. O. & Gordon, S. The M1 and M2 paradigm of macrophage activation: time for reassessment. *F1000Prime Rep.* **6**, 13 (2014).
67. Arnold, L. et al. CX3CR1 deficiency promotes muscle repair and regeneration by enhancing macrophage ApoE production. *Nat. Commun.* **6**, 8972 (2015).
68. Wang, Y. et al. Tissue-resident macrophages promote extracellular matrix homeostasis in the mammary gland stroma of nulliparous mice. *eLife* **9**, e57438 (2020).
69. Li, C., Levin, M. & Kaplan, D. L. Bioelectric modulation of macrophage polarization. *Sci. Rep.* **6**, 21044 (2016).
70. Hoare, J. I., Rajnicek, A. M., McCaig, C. D., Barker, R. N. & Wilson, H. M. Electric fields are novel determinants of human macrophage functions. *J. Leukoc. Biol.* **99**, 1141–1151 (2016).

Publisher's note Springer Nature remains neutral with regard to jurisdictional claims in published maps and institutional affiliations.

Springer Nature or its licensor (e.g. a society or other partner) holds exclusive rights to this article under a publishing agreement with the author(s) or other rightsholder(s); author self-archiving of the accepted manuscript version of this article is solely governed by the terms of such publishing agreement and applicable law.

© The Author(s), under exclusive licence to Springer Nature America, Inc. 2022

¹Department of Chemical Engineering, Stanford University, Stanford, CA, USA. ²Department of Surgery, Division of Plastic and Reconstructive Surgery, Stanford University School of Medicine, Stanford, CA, USA. ³Department of Biology, Stanford University, Stanford, CA, USA. ⁴BOE Technology Center, BOE Technology Group Co., Ltd, Beijing, China. ⁵Stanford Distinguished Careers Institute, Stanford University, Stanford, CA, USA. ⁶Department of Genetics, Stanford University School of Medicine, Stanford, CA, USA. ⁷Department of Surgery, University of Arizona College of Medicine, Tucson, AZ, USA. ⁸Department of Materials Science and Engineering, Stanford University, Stanford, CA, USA. ⁹These authors contributed equally: Yuanwen Jiang, Artem A. Trotsyuk, Simiao Niu. ✉e-mail: ggurtner@stanford.edu; zbao@stanford.edu

Methods

Fabrication of the flexible circuit

Flexible printed circuit boards with custom designs were manufactured by commercial vendors under the ISO 9001 certificate; for example, PCBWay. The bill of materials includes passive components (capacitors, resistors and diodes), a thermistor (no. 103KT1608T-1P, Semitec), an ISO 15693 sensor transponder with a programmable low-power microcontroller (no. RF430FRL152H, Texas Instruments), a crystal oscillator (no. SG-3040LC 32.7680KB3: PURE SN, Epson Timing) and two operational amplifiers (no. TSV620AILT, STMicroelectronics). All circuit components were soldered using tin-lead solder paste (no. Sn63/Pb37, melting point 183 °C; 247 Solder) by hot-air blowing.

To avoid chronic electrochemical corrosion of the electroless nickel immersion gold electrodes on the rear aspect of the smart bandage board (two for stimulation, two for sensing), silver/silver chloride (Ag/AgCl) conducting paste (no. Cl-4040, Nagase ChemteX) was printed onto each electrode using blades and cured on a hot plate at 100 °C for 10 min. The electrode area was further encapsulated by an elastomeric polyurethane coating (Clear Flex 50, mix ratio 1A/2B wt/wt; Smooth-On) and cured at 70 °C for 15 min. The hydrogel interface electrodes were then placed onto corresponding Ag/AgCl electrodes for sensing and stimulation purposes.

For smart bandage preparation, PCB board manufacture and shipping requires about 7 days and soldering and gel preparation steps one further day; total production time is thus about 8 days. The electronics themselves are also completely reusable. For a batch of 50 FPCB boards the total expense is typically -US\$150, with each device costing -US\$3. All electronic components soldered to the device cost -US\$13. For the hydrogel electrode, the material cost is -US\$2 per device. The overall cost is thus -US\$18 per smart bandage.

The resonant frequency and quality factor of the antenna were measured using a portable VNA (miniVNA Tiny Plus 2). The resonant frequency was determined by the peak location of impedance amplitude. The quality factor was calculated by resonant frequency divided by the 3-dB bandwidth.

Synthesis of conducting adhesive hydrogel

In a typical synthesis, 40 mg of PEDOT:PSS dry pellet (Orgacon DRY5, Agfa), 300 mg of NIPAM (Sigma-Aldrich), 24 mg of AAm (Sigma-Aldrich) and 1 mg of *N,N'*-methylenebisacrylamide (MBAA, Sigma-Aldrich) were mixed and dissolved in 2 ml of water by grinding in an agate mortar to form a viscous suspension. Before gel initiation, 50 µl of 30% (v/v) hydrogen peroxide (H₂O₂, Fisher Scientific) and 50 µl of 20% (wt/vol) ascorbic acid (AA, Sigma-Aldrich) were added sequentially to the monomer mixture and quickly mixed before pouring into Teflon molds for subsequent gelation at room temperature.

For the control sample without PEDOT:PSS, the same procedure was performed except for the absence of the PEDOT:PSS pellet in the initial mixture. For the study of AAm content on overall LCST behavior, the initial amount of AAm was varied between 0, 18, 24 and 30 mg. For the study of electrochemical properties, the initial amount of PEDOT:PSS was varied between 0, 10, 20, 30 and 40 mg. For the study of crosslinking density, the initial amount of MBAA was varied between 0.3, 1, 3 and 10 mg.

Hydrogels were stored in sealed and moisturized bags at 4 °C to avoid evaporation of water. Under this storage condition, gels can maintain a stable hydration level for at least 4 weeks. We did not evaluate longer-term storage. The hydrogel electrodes were placed at the periphery of the wound with one pair for stimulation and a second for impedance sensing. Because of the position of the hydrogel (periphery of the wound), it was not in direct contact with wound fluid itself and, as a result, we did not encounter severe biofouling in our experiment. The skin hydration level of mice is typically stable in controlled housing and laboratory environments, and thus we did not account for this factor in our measurements. Regarding contact pressure, because of

the high adhesion of our hydrogel electrode it can be attached stably to the skin with consistent contact impedance and therefore we did not need to control for contact pressure.

Electrochemical characterization

EIS was performed using the hydrogel as the working electrode, platinum as the counter electrode, Ag/AgCl as the reference electrode and PBS as the electrolyte. Impedance and phase angle as functions of frequency were acquired by a Bio-Logic VSP-300 workstation with sine wave signal amplitude of 10 mV. Chronoamperometry was performed on the same potentiostat by delivering biphasic square-wave pulses with 50 ms for each phase and 100 mV amplitude, with currents being recorded simultaneously.

Conductivity measurements were carried out using a four-point probe method with a Keithley 4200 SC semiconductor analyzer. For the measurement of impedance change over strain, the conducting hydrogel was mounted on a home-made automated stretcher on which impedance values at different strain levels were recorded using a LCR meter (Keysight Technologies, no. E4098A).

Mechanical characterization

Unidirectional tensile tests of the hydrogel electrodes were performed on an Instron 5565 at a strain rate of 10 mm min⁻¹. To measure interfacial energy, hydrogel samples and surfaces for adhesion (for example, metal, plastic, rubber and skin) were glued using cyanoacrylate (Krazy Glue) onto Kapton polyimide films as a stiff backing. After adherence of the hydrogel onto the surface of interest, adhesion was tested by the standard 180° peel test with the Instron machine. All tests were conducted with a constant peeling speed of 10 mm min⁻¹. Interfacial toughness was calculated by dividing twice the plateau by the width of the tissue sample. DSC was conducted using a TA Instruments Q2000 DSC. Rheological measurements were performed using a TA Instruments ARES-G2 rheometer.

Hydrogel biocompatibility assay

All tissue sample histology slides were examined via light microscopy by the study pathologist. Wound sites were semiquantitatively scored according to the criteria shown in Supplementary Table 2.

Semiquantitative scores were assigned based on the representative site response observed over six noncontiguous, representative, high-power microscope fields at the host–test sample interface. Test sample (with gel) and control sample (without gel) scored results were documented by animal, as shown in Supplementary Fig. 19. Sample reactivity score calculations were documented and categorized. Representative low- and high-magnification implant site photomicrographs are shown in Supplementary Fig. 19. After scoring of each implant site sample or subsample slide section, the following steps were performed. Polymorphonuclear cells, lymphocytes, plasma cells, macrophages, giant cells and necrosis scores assigned for each implant were totaled and multiplied by two (subtotal A); neovascularization, fibrosis and fatty infiltration scores assigned for each implant were totaled (subtotal B), then subtotals A and B were summed to yield total implant score (total). For each test or control sample type, total values were summed (group total). Each group total was averaged (group average) by the appropriate number of scored implants. Control group average was subtracted from test group average to derive the final average test result (test sample relative score). A resulting negative difference was recorded as zero, according to the protocol. Test sample relative score, according to Supplementary Fig. 19, was used to categorize the test sample.

Animal testing

Animals. Female mice 8–12 weeks old (eC57BL/6J, Jackson Laboratory) were housed in the Stanford University Veterinary Service Center in accordance

with National Institutes of Health (NIH) and institution-approved animal care guidelines. Housing conditions consisted of a maximum of five mice per cage with a 12/12-h light/dark cycle, temperatures of 65–75 °F and 40–60% humidity. Mice within one experiment were of the same strain, batch and birthday. All procedures were approved by the Stanford Administrative Panel on Laboratory Animal Care.

Open-field movement test. The open-field test for mice with and without the smart bandage was performed in a 25 × 40-cm² open cage. Four mice per group were allowed to freely explore the open-field enclosure for 15 min under ambient conditions while being recorded by an overhead camera. The recorded videos were analyzed using DeepLabCut (v.2.2) deep learning architecture to measure total travel distances for each group.

Excisional splinted wound model. Twelve-week-old C57BL/6 mice (Jackson Laboratories) were randomized into the following groups: (1) stimulated and (2) nonstimulated control ($n = 5$). Excisional wounds on the dorsum were created using 6-mm biopsy punches as previously described⁷¹. Wounds were treated daily until closure. All wounds were covered with an occlusive dressing (Tegaderm, 3 M). The healing experiment was performed using rectified AC signals at 13.56 MHz with the voltage oscillating between 0 and 2 V. Wounds were treated daily for 6 h using the wireless smart bandage. Dressing changes were conducted in between daily treatment episodes. Digital photographs of the wounds were taken every day until closure. Wound closure was defined as the time at which the wound was completely re-epithelialized without any scab. Wound area was determined using ImageJ (v.10.2) software by a blinded observer (NIH).

Contact-burn model. An established partial-thickness contact-burn model was used⁷². Briefly, mice were anesthetized using 2% isoflurane and administered 0.05 mg kg⁻¹ buprenorphine subcutaneously. Aluminum cylinders (10-mm diameter; Alfa Aesar) were heated in a 100 °C water bath for 5 min and applied to the dorsa of the animals for 15 s, with only the weight of the rod (47.75 g) applying pressure to the skin. Two burns were created on each mouse. Mice were immediately placed supine in a cool water bath for 1 min to quench the burn. Wounds were mechanically debrided on post-burn day 5 using a blunt stainless steel rod and randomized to either treatment with stimulation or no treatment (no stimulation) ($n = 4$ for each group). The healing experiment was performed using rectified AC signals at 13.56 MHz with the voltage oscillating between 0 and 2 V. Wounds were treated daily for 6 h using the wireless smart bandage. Dressing changes were conducted in between daily treatment episodes. Burns were photographed at regular intervals until completely healed, and analyzed using ImageJ (v.10.2) software (NIH). Wound area (as percentage of original) was plotted against post-burn day with area under the curve.

STZ-induced wound model. To model type I diabetic wound healing, an STZ-induced mouse model was used⁴⁶. Eight-week-old C57BL/6 mice were fed high-fat, high-sugar feed and maintained under a specific-pathogen-free environment. Briefly, STZ (100 mg kg⁻¹; Sigma-Aldrich) was mixed in sodium citrate buffer (intraperitoneal injection) and administered daily for two consecutive days ($n = 4$ for each group, stimulated and nonstimulated control). All mice with plasma glucose levels ≥16.7 mM under normal conditions were considered diabetic 2 weeks after the first STZ injection⁴⁵. Animals were maintained in a diabetic state for the duration of the experiment. The healing experiment was performed using rectified AC signals at 13.56 MHz with the voltage oscillating between 0 and 2 V. Wounds were treated daily for 6 h using the wireless smart bandage. Dressing changes were conducted in between daily treatment episodes.

Infection model. To validate the effectiveness of electrical stimulation at reducing biofilm and wound infection, an *Escherichia coli* wound

infection model was used⁷³. Briefly, 30 µl of fresh culture of *E. coli* DH5-α was inoculated overnight in 10 ml of lysogeny broth (LB) medium. *E. coli* was grown at 37 °C with shaking to an optical density (OD) of 600. After overnight incubation, tubes were vortexed and the volume adjusted to obtain 10⁷ colony-forming units (CFU) ml⁻¹. Bacteria were centrifuged and resuspended in 20 ml of sterile PBS. To control bacterial concentration, a serial dilution of the utilized suspension was prepared and inoculated on a fresh LB agar plate followed by incubation for 18 h at 37 °C. Colonies were counted the next day to determine the original bacterial concentration.

On the day of inoculation, 6-mm excisional wounds were created on the mouse dorsum and inoculated with 10 µl of PBS containing 10⁷ CFU bacteria using a pipette tip. Tegaderm (3 M) were cut and applied to the wound area. Wounds were either treated with continuous stimulation or left untreated. Immediately after treatment, the wound and its periphery were swabbed with a BD ESwab Collection & Transport System (BD Biosciences) and submitted to Stanford Diagnostic Laboratory for quantification. $n = 5$ was submitted for each treatment group at time points 0, 24 and 72 h post inoculation.

A semiquantitative method was used to enumerate total bacterial colony count. A sample was plated from the ESwab fluid then spread into quadrants. If bacteria grew where the original specimen was plated, that is referred to as 1+ growth (or very light colony growth); 2+ extends to the edges of the first quadrant and outside the 1+ region (light colony growth), 3+ is considered moderate colony growth and is colony growth that extends through the 3rd quadrant, while 4+ is heavy colony growth and grows into the 4th quadrant. Data were subsequently aggregated and analyzed. Digital photographs of the wounds were taken every day of specimen collection.

Parabiosis model. To study the role of cell migration into the wound, a parabiosis model was used as previously described⁷⁴. Briefly, the corresponding flanks of GFP⁺ (C57BL/6-Tg(CAG-EGFP)1Osb/J) and C57BL/6J mice (WT) were shaved and disinfected with Betadine solution and 70% ethanol three times. Matching skin incisions were made from the olecranon to the knee joint of each mouse. The skin edges were undermined to create skin flaps of width 1 cm. Nylon sutures (6–0; Ethilon) were used to approximate the dorsal and ventral edges of the skin flaps, and skin staples were used to close longitudinal incisions. Buprenorphine was used for analgesia by subcutaneous injection every 8–12 h for 48 h postoperatively. Mice were monitored daily until the end of the experiment. After 14 days, peripheral blood chimerism was confirmed using fluorescent microscopy of tail vein blood. After cross-circulation was established between the two parabionts, an excisional splinted wound was created on the dorsum of WT mice. Wounds are subsequently treated with stimulation or left untreated; $n = 5$ for each group.

On day 5, analysis of murine cells isolated from excisional wounds was performed according to published protocols for flow cytometry on murine tissue⁷⁵. Briefly, tissue was explanted on day 5 from the parabiosis model then microdissected and incubated in serum-free DMEM with 240 U ml⁻¹ of collagenase administered intravenously for 1 h at 37 °C in a rotating oven. Digested tissue was filtered, centrifuged and stained with PE/Cy7 rat anti-mouse CD11b antibody (no. 101216, Biolegend, 1:100), PE rat anti-mouse CD163 antibody (no. 156704, Biolegend, 1:100) and APC rat anti-mouse F4/80 antibody (no. 123116, Biolegend, 1:100). DAPI was used to stain dead cells. Flow cytometry was performed on a BD fluorescent activated cell sorting (FACS) Aria (Becton Dickinson), and data were analyzed using FlowJo (v.10.5.3) (Becton Dickinson). GFP⁺ cells from stimulated and nonstimulated control groups were sorted into collection tubes and submitted for 10X sequencing. The experiment was performed using rectified AC signals at 13.56 MHz, with the voltage oscillating between 0 and 2 V. Wounds were treated daily for 6 h using the wireless smart bandage. Dressing changes were conducted in between daily treatment episodes.

Skin impedance and temperature sensing. The smart bandage was attached to the mouse skin interfaced by the hydrogel electrodes. Continuous wireless readout of temperature and impedance was performed using a 13.56-MHz desktop reader/writer with built-in antenna (no. 233015, Gao RFID). Software provided by the vendor (DevMgr, Gao RFID) was used to control readout sampling interval and data storage. An infrared (IR) thermal imaging camera (HT-19, Hti-Xintai) was used to capture thermal mouse images.

Tissue characterization

Histology and staining. Wounds were harvested with a 2-mm rim of nonwounded skin from euthanized mice. Skin tissues were fixed overnight in 4% paraformaldehyde followed by serial dehydration in ethanol and embedding in paraffin, as previously described⁷¹. Sections of 5 µm ($n = 5$) were stained with hematoxylin and eosin (H&E) and Masson's trichrome (Sigma-Aldrich). Nuclei were stained with Hoechst dye. Tissue was stained for picrosirius red (Sigma-Aldrich). For CD31 (no. ab28364, Abcam, 1:50), α-SMA (no. ab5694, Abcam, 1:100), CD206 (no. ab64693, Abcam, 1:100) and CD163 (no. ab182422, Abcam, 1:500), DAPI (no. ab104139, Abcam) was used to stain for nuclei.

For immunohistochemical staining, slides were first deparaffinized in xylene and then rehydrated in ethanol/PBS mixtures. The slides were then washed three times in PBS. Next, the slices underwent antigen retrieval using 1× sodium citrate pH 6.0 (100× diluted in PBS; Abcam) in deionized (DI) H₂O. The slices, submerged in the solution, were warmed in a microwave on full power for 90 s; 1 min later, at 60% power for 60 s; 1 min later, the slices in solution were placed in a temperature of 4 °C for 30 min and subsequently soaked in DI H₂O for 5 min. The slices were then washed three times in PBS.

Slices were permeabilized for intracellular antigens with 0.2% Triton X-100 (Sigma-Aldrich) for 10 min then washed three times with PBS. A PAP/hydrophobic pen was used to isolate slices, which were then blocked with a solution consisting of 5% goat serum (vol/vol; Sigma-Aldrich) in PBS for 2 h at room temperature in a humidified chamber.

Slices were then incubated for 1 day at 4 °C with primary antibodies in blocking solution. Sections were washed three times with PBS for 30 min and stained for 2 h at 4 °C with corresponding secondary antibodies (goat anti-mouse IgG (H + L) Highly Cross-Adsorbed Secondary Antibody, Alexa Fluor Plus 488, no. A32723, 1:25, ThermoFisher; and goat anti-rabbit IgG (H + L) Highly Cross-Adsorbed Secondary Antibody, Alexa Fluor Plus 647, no. A32733, 1:250, ThermoFisher). Slices were washed three times with PBS and incubated with DAPI (1:50,000) for 30 min.

H&E and Masson's trichrome were imaged with brightfield microscopy. Picrosirius red was imaged using polarized light microscopy (Leica DM5000 B upright microscope) to obtain ×40 magnification images. CD31, α-SMA, CD206 and CD163 were imaged using a Zeiss LSM 880 confocal laser scanning microscope at the Cell Science and Imaging Facility at Stanford University. To obtain high-resolution images of tissue samples, multiple images at ×25 magnification were acquired using automatic tile scanning and were stitched together using Leica LAS-X software.

Tissue analysis. ImageJ (NIH) was used to binarize images taken with the same settings, and intensity thresholds were used to quantify staining based on pixel-positive area averaged over three high-power fields. All histologic and immunofluorescent images shown are representative images of multiple experiments, and were performed by a blinded observer. Dermal thickness was quantified using Image J, where the distance from the epidermis to the dermis, visible in red with Masson's trichrome, was measured. Luminal structures, visible with Masson's trichrome staining, containing red blood cells were considered dermal microvessels. Three high-power fields at ×40 were examined for each wound sample to quantify microvessels. Appendages were quantified using Masson's trichrome with three high-power fields at ×5.

Dermal collagen analysis. Picosirius red images were used for the following analysis. The CT-FIRE algorithm (v.10.2) was used to analyze individual fiber metrics including length, width, angle and curvature. This can also extract other variables such as localized fiber density and the spatial relationship between fiber and the associated boundary⁷⁶. CurveAlign 4.0 was used to quantify all fiber angles and strength of alignment within an image⁷⁷. Complexity and heterogeneity were measured using the ImageJ plug-in FracLac (v.2.5)⁷⁸. Local fractal dimensions (FD) and lacunarity (L) values were calculated using the subsample box counting scan (50-grid default sampling size, minimum pixel density threshold 0, rectangle subscan). FD measures density of collagen networks; a higher FD has a denser and scar-like fiber arrangement. L measures the amount of randomness or heterogeneity in a sample; a low L implies less heterogeneous collagen fiber orientation. Finally, MatFiber was used to further quantify fiber alignment, reported as mean vector length. The strength of alignment ranges from a value of 0 (completely random fiber alignment) to 1 (completely aligned fibers)⁷⁹. The average fiber parameters for each mouse were used for statistical analysis.

Wound tensile testing. Biomechanical testing was performed as previously described⁸⁰. Briefly, uniaxial tensile testing was performed at room temperature using a tensile testing apparatus (Instron 5565). Constant volume deformation was assumed during uniaxial stretching.

In vitro study of cell alignment and migration

Human umbilical vein endothelial cells (HUVEC, Sigma-Aldrich) were cultured on glass-bottomed Petri dishes and passaged following standard procedures from the vendor.

For the alignment/migration study, a silicone spacer based on polydimethylsiloxane (25 × 5 × 10 mm³, L × W × H) was glued to a glass-bottomed dish using a biocompatible silicone adhesive (Kwik-Sil, World Precision Instruments) with a small opening at the bottom (5 mm × 5 mm × 200 µm, L × W × H) to allow medium exchange and establish the electric field. HUVEC cells were seeded in the opening of the spacer to allow adherence of cells and their proliferation for 24 h. Cells were then stained with 2 µM Calcein AM (ThermoFisher) for 30 min at 37 °C and washed three times with dye-free culture medium before imaging.

During the experiment, using an agar salt bridge, a waveform-mimicking wireless stimulation condition was applied with a 13.56-MHz sinusoidal wave of 1-V peak-to-peak amplitude. Live cells were imaged in real time using a Leica TCS SP8 confocal microscope (Leica) and analyzed with ImageJ (v.10.2) software.

Single-cell analysis

scRNA-seq. The GFP⁺ cell suspension was resuspended in a concentrated solution and submitted for droplet-based microfluidic scRNA-seq at the Stanford Functional Genomics Facility using the 10X Chromium Single Cell platform (Single Cell 3' v.3, 10X Genomics). The cell suspension, reverse-transcription master mix and partitioning oil were loaded onto a single-cell chip, processed on the Chromium Controller, and reverse transcription was performed at 53 °C for 45 min. Complementary DNA was amplified for 12 cycles in total (BioRad C1000 Touch thermocycler) with cDNA size selected using SpriSelect beads (Beckman Coulter) and a 3:5 ratio of SpriSelect reagent volume to sample volume. cDNA was analyzed on an Agilent Bioanalyzer High Sensitivity DNA chip for qualitative control and fragmented for 5 min at 32 °C, followed by end repair and A-tailing at 65 °C for 30 min and double-sided size selection with SpriSelect. Sequencing adapters were ligated to the cDNA at 20 °C for 15 min. cDNA was amplified using a sample-specific index oligo as primer, followed by another round of double-sided size selection. Final libraries were analyzed on an Agilent Bioanalyzer High Sensitivity DNA chip for qualitative control.

purposes. cDNA libraries were sequenced on a HiSeq 4000 Illumina platform, aiming for 50,000 reads per cell.

scRNA-seq data processing, normalization and cell cluster identification. Base calls were converted to reads using the Cell Ranger (10X Genomics, v.3.1) implementation `mkfastq` and then aligned against the MM 10 (mouse) genome using Cell Ranger's count function with SC3Pv3 chemistry and 5,000 expected cells per sample. Cell barcodes representative of quality cells were delineated from barcodes of apoptotic cells or background RNA based on a threshold of having at least 300 unique transcripts profiled, <100,000 total transcripts and <10% of their transcriptome of mitochondrial origin. Unique molecular identifiers (UMIs) from each cell barcode were retained for all downstream analysis. Raw UMI counts were normalized with a scale factor of 10,000 UMIs per cell and subsequently natural log transformed with a pseudocount of 1 using the R package Seurat (v.3.1.1)⁸¹. Aggregated data were then evaluated using UMAP analysis over the first 15 principal components⁸². Cell annotations were ascribed using the SingleR package (v.3.11) against the ImmGen database^{83,84}, and confirmed by expression analysis of specific cell type markers. Louvain clustering was performed using a resolution of 0.5 and 15 nearest neighbors. Cell type markers were generated using Seurat's native `FindMarkers` function with a log fold change threshold of 0.25, using receiver operating characteristic to assign predictive power to each gene.

Pseudotime analysis. Pseudotime analysis was performed using the Monocle 3 package in R (v.3.0.2.0)⁸⁵. A principal graph was learned from the reduced dimension space using reversed-graph embedding with default parameters. The principal GraphTest function using Moran's *I*-statistic was employed to identify correlated genes on trajectory embedded in the manifold.

RNA velocity analysis. RNA velocity analysis was performed using scVelo (v.0.2.5)⁵⁹. In contrast to previous steady-state models, which falsely assume that all genes share a common splicing rate, scVelo uses a likelihood-based dynamical model to solve the full transcriptional dynamics of splicing kinetics. Thereby RNA velocity analysis can be adapted to transient cell states and heterogeneous cellular subpopulations as in our dataset. Partition-based graph abstraction was performed using the `sc.tl.paga` function in scVelo. To find genes with differentially regulated transcriptional dynamics compared with all other clusters, a Welch *t*-test with conservative overestimated variance was applied using the function `sc.tl.rank_velocity_genes`. Genes were ranked by their likelihood obtained from the dynamical model grouped by Seurat clusters. A pseudotime heatmap was created by plotting the expression of genes identified by `sc.tl.rank_velocity_genes` along velocity-inferred pseudotime. The terminal transcriptional states were identified as end points of the velocity-inferred Markov diffusion process.

CytoTRACE. CytoTRACE was used to infer cell differentiation trajectories^{86,87}. Briefly, this algorithm places cells along a trajectory corresponding to a biological process (cell differentiation) by taking advantage of an individual cell's asynchronous progression under an unsupervised framework.

Statistical analysis

Statistical significance was determined using a two-tailed unpaired *t*-test for experiments involving only two conditions. For experiments with three or more conditions, pairwise *t*-tests were employed, and *P* values adjusted using Bonferroni correction for multiple hypothesis testing. *P*<0.05 was considered statistically significant. The statistical methods used for scRNA-seq analysis are described in the specific sections above.

Reporting summary

Further information on research design is available in the Nature Research Reporting Summary linked to this article.

Data availability

The authors declare that all data supporting the findings of this study are available within the paper and its supplementary information.

References

71. Duscher, D. et al. Aging disrupts cell subpopulation dynamics and diminishes the function of mesenchymal stem cells. *Sci. Rep.* **4**, 7144 (2014).
72. Tavares Pereira, Do, S., Lima-Ribeiro, M. H., de Pontes-Filho, N. T., Carneiro-Leão, A. M. & Correia, M. T. Development of animal model for studying deep second-degree thermal burns. *J. Biomed. Biotechnol.* **2012**, 460841 (2012).
73. Fila, G. et al. Murine model imitating chronic wound infections for evaluation of antimicrobial photodynamic therapy efficacy. *Front. Microbiol.* **7**, 1258 (2016).
74. Wong, V. W., Sorkin, M., Glotzbach, J. P., Longaker, M. T. & Gurtner, G. C. Surgical approaches to create murine models of human wound healing. *J. Biomed. Biotechnol.* **2011**, 969618 (2011).
75. Walmsley, G. G. et al. Murine dermal fibroblast isolation by FACS. *J. Vis. Exp.* **107**, e53430 (2016).
76. Liu, Y., Keikhosravi, A., Mehta, G. S., Drifka, C. R. & Eliceiri, K. W. Methods for quantifying fibrillar collagen alignment. *Methods Mol. Biol.* **1627**, 429–451 (2017).
77. Bredfeldt, J. S. et al. Computational segmentation of collagen fibers from second-harmonic generation images of breast cancer. *J. Biomed. Opt.* **19**, 16007 (2014).
78. Kam, Y. et al. Nest expansion assay: a cancer systems biology approach to in vitro invasion measurements. *BMC Res. Notes* **2**, 130 (2009).
79. Chen, K. et al. Role of boundary conditions in determining cell alignment in response to stretch. *Proc. Natl Acad. Sci. USA* **115**, 986–991 (2018).
80. Wong, V. W. et al. Focal adhesion kinase links mechanical force to skin fibrosis via inflammatory signaling. *Nat. Med.* **18**, 148–152 (2011).
81. Stuart, T. et al. Comprehensive integration of single-cell data. *Cell* **177**, 1888–1902 (2019).
82. Diaz-Papkovich, A., Anderson-Trocmé, L., Ben-Eghan, C. & Gravel, S. UMAP reveals cryptic population structure and phenotype heterogeneity in large genomic cohorts. *PLoS Genet.* **15**, e1008432 (2019).
83. Mostafavi, S. et al. Variation and genetic control of gene expression in primary immunocytes across inbred mouse strains. *J. Immunol.* **193**, 4485–4496 (2014).
84. Aran, D. et al. Reference-based analysis of lung single-cell sequencing reveals a transitional profibrotic macrophage. *Nat. Immunol.* **20**, 163–172 (2019).
85. Trapnell, C. et al. The dynamics and regulators of cell fate decisions are revealed by pseudotemporal ordering of single cells. *Nat. Biotechnol.* **32**, 381–386 (2014).
86. Li, D. Q. et al. Single-cell transcriptomics identifies limbal stem cell population and cell types mapping its differentiation trajectory in limbal basal epithelium of human cornea. *Ocul. Surf.* **20**, 20–32 (2021).
87. Gulati, G. S. et al. Single-cell transcriptional diversity is a hallmark of developmental potential. *Science* **367**, 405–411 (2020).

Acknowledgements

This work was supported by the Stanford Clinical and Translational Science Award (CTSA) to Spectrum. The CTSA program is led by the National Center for Advancing Translational Sciences at NIH.

Part of this work was performed at Stanford Nano Shared Facilities, supported by the National Science Foundation under award no. ECCS-2026822. We thank Agfa for providing PEDOT:PSS. We thank T. Carlonagno and T. Vang for administrative support. We thank Y. J. Park for tissue histology support, and D. Wu at Stanford Animal Histology Services and P. Chu at the Human Research Histology Core for help with preparation of histologic specimens. We thank S. Kananian for instrument support with VNA measurements. We also thank R. Altman for his guidance with the project.

Author contributions

Y.J., A.A.T., S.N., G.C.G. and Z.B. designed the study. S.N. and Y.J. performed circuit design and testing. Y.J., C.-C.S., J.-C.L., D.Z. and J.T. performed material synthesis and characterizations. A.A.T., Y.J., D.H., K.C., A.M.M.-B., S.M., M.R.L., A.S., E.B., S.J., S.R.S., K.S., T.J., E.Z., C.R.N., W.G.V., D.S., J.P., M.R., D.P.P., A.C., M.C.L., C.A.B., S.H.K., K.S.F., G.G., K.L. and K.Z. performed animal and cell culture experiments and single-cell evaluations. Y.J., A.A.T., S.N., M.J., G.C.G. and Z.B. wrote the manuscript with input from all coauthors.

Competing interests

Y.J., A.A.T., S.N., G.C.G. and Z.B. have filed a provisional application of patent through Stanford University with the assigned application number 63/238,017. The remaining authors declare no competing interests.

Additional information

Supplementary information The online version contains supplementary material available at <https://doi.org/10.1038/s41587-022-01528-3>.

Correspondence and requests for materials should be addressed to Geoffrey C. Gurtner or Zhenan Bao.

Peer review information *Nature Biotechnology* thanks Can Dincer and the other, anonymous, reviewer(s) for their contribution to the peer review of this work.

Reprints and permissions information is available at www.nature.com/reprints.

Reporting Summary

Nature Research wishes to improve the reproducibility of the work that we publish. This form provides structure for consistency and transparency in reporting. For further information on Nature Research policies, see our [Editorial Policies](#) and the [Editorial Policy Checklist](#).

Statistics

For all statistical analyses, confirm that the following items are present in the figure legend, table legend, main text, or Methods section.

n/a Confirmed

- The exact sample size (n) for each experimental group/condition, given as a discrete number and unit of measurement
- A statement on whether measurements were taken from distinct samples or whether the same sample was measured repeatedly
- The statistical test(s) used AND whether they are one- or two-sided
 - Only common tests should be described solely by name; describe more complex techniques in the Methods section.*
- A description of all covariates tested
- A description of any assumptions or corrections, such as tests of normality and adjustment for multiple comparisons
- A full description of the statistical parameters including central tendency (e.g. means) or other basic estimates (e.g. regression coefficient) AND variation (e.g. standard deviation) or associated estimates of uncertainty (e.g. confidence intervals)
- For null hypothesis testing, the test statistic (e.g. F , t , r) with confidence intervals, effect sizes, degrees of freedom and P value noted
 - Give P values as exact values whenever suitable.*
- For Bayesian analysis, information on the choice of priors and Markov chain Monte Carlo settings
- For hierarchical and complex designs, identification of the appropriate level for tests and full reporting of outcomes
- Estimates of effect sizes (e.g. Cohen's d , Pearson's r), indicating how they were calculated

Our web collection on [statistics for biologists](#) contains articles on many of the points above.

Software and code

Policy information about [availability of computer code](#)

Data collection	Wireless readout and stimulation was performed using a 13.56 MHz desktop reader/writer with built-in antenna (233015, Gao RFID). Software provided by the vendor (DevMgr, Gao RFID) was used to control the readout sampling interval and data storage.
Data analysis	<p>For the open-field test for mice with and without the smart bandage, the recorded videos were analyzed using the DeepLabCut (v. 2.2) deep learning architecture to measure the total travel distances for each group. For the excisional splinted wound model, wound area was determined using ImageJ software (v. 10.2) by a blinded observer (NIH, Bethesda, MD). For the contact burn model, photographs of burns were analyzed using ImageJ software (v. 10.2).</p> <p>For the parabiosis model, flow cytometry data was analyzed using FlowJo (v. 10.5.3) (Becton Dickinson, San Jose, CA).</p> <p>For tissue analysis, Image J (v. 10.2) was used to binarize images taken with the same settings, and intensity thresholds were used to quantify staining based upon pixel-positive area averaged over three high power fields. ImageJ (v. 10.2) was also used to quantify dermal thickness.</p> <p>For dermal collagen analysis, the CT-FIRE algorithm (v. 2.0) was used to analyze individual fiber metrics such as length, width, angle, and curvature. CurveAlign 4.0 was also used to quantify all fiber angles and strength of alignment within an image. Complexity and heterogeneity were measured using the ImageJ plug-in FracLac (v. 2.5). Lastly, MatFiber was used to further quantify fiber alignment, reported as mean vector length.</p> <p>For the alignment/migration study of HUVEC cells, live cells were imaged in real time using a Leica TCS SP8 confocal microscope (Leica) and analyzed using ImageJ (v. 10.2) software.</p> <p>For single cell RNA-seq data processing, normalization, and cell cluster identification, raw unique molecular identifier counts were normalized and subsequently natural log transformed with a pseudocount of 1 using the R package Seurat (version 3.1.1). Cell annotations were ascribed using the SingleR package (version 3.11) against the ImmGen database. Louvain clustering was performed using a resolution of 0.5 and 15</p>

nearest neighbors. Cell-type markers were generated using Seurat's native FindMarkers function.

For pseudotime analysis, the Monocle 3 package in R (version 3.0.2.0) was used. The principal GraphTest function using the Moran's I statistic was also employed to identify correlated genes on trajectory embedded in the manifold.

For RNA velocity analysis, scVelo (v. 0.5.5) was used.

CytoTRACE (Cellular Trajectory Reconstruction Analysis using gene Counts and Expression) was also used to infer the cell differentiation trajectories.

For manuscripts utilizing custom algorithms or software that are central to the research but not yet described in published literature, software must be made available to editors and reviewers. We strongly encourage code deposition in a community repository (e.g. GitHub). See the Nature Research [guidelines for submitting code & software](#) for further information.

Data

Policy information about [availability of data](#)

All manuscripts must include a [data availability statement](#). This statement should provide the following information, where applicable:

- Accession codes, unique identifiers, or web links for publicly available datasets
- A list of figures that have associated raw data
- A description of any restrictions on data availability

The authors declare that all data supporting the findings of this study are available within the paper and its supplementary information.

Field-specific reporting

Please select the one below that is the best fit for your research. If you are not sure, read the appropriate sections before making your selection.

Life sciences Behavioural & social sciences Ecological, evolutionary & environmental sciences

For a reference copy of the document with all sections, see nature.com/documents/nr-reporting-summary-flat.pdf

Life sciences study design

All studies must disclose on these points even when the disclosure is negative.

Sample size	Sample size was determined by the number of biological and technical replicates necessary for each experiment. The number of biological replicates was a minimum of 3, with several technical replicates in each sample, sufficient to satisfy criteria for statistical analyses on the resulting data collected. Specifically, sample sizes were determined empirically based on the authors' extensive experience with scRNA-seq, from which we and the broader community have found that minimum n=3 biological replicates is almost always appropriate for syngeneic animal studies. ARRIVE 2.0 guidelines (Animal Research: Reporting of In Vivo Experiments) were used to maximize quality and reliability of research reported.
Data exclusions	No data were excluded from the analyses.
Replication	All experimental findings, including chemical synthesis, material characterizations, and animal experiments, were reliably reproduced with time intervals over at least three months.
Randomization	Experimental groups were formed based on what was being tested with random selection. Mice within one experiment were of the same strain, batch, and birthday. Mice were allocated to different experimental arms of a study using the ARRIVE 2.0 guidelines (Animal Research: Reporting of In Vivo Experiments).
Blinding	All histology and immunofluorescent images shown are representative images of multiple experiments and were performed by a blinded observer. Wound area in the excisional splinted wound model was determined using ImageJ software by a blinded observer (NIH, Bethesda, MD). For the rest of the experiments listed in our study, investigators were blinded to group allocation during data collection and analysis.

Reporting for specific materials, systems and methods

We require information from authors about some types of materials, experimental systems and methods used in many studies. Here, indicate whether each material, system or method listed is relevant to your study. If you are not sure if a list item applies to your research, read the appropriate section before selecting a response.

Materials & experimental systems

n/a	Involved in the study
<input type="checkbox"/>	<input checked="" type="checkbox"/> Antibodies
<input type="checkbox"/>	<input checked="" type="checkbox"/> Eukaryotic cell lines
<input checked="" type="checkbox"/>	<input type="checkbox"/> Palaeontology and archaeology
<input type="checkbox"/>	<input checked="" type="checkbox"/> Animals and other organisms
<input checked="" type="checkbox"/>	<input type="checkbox"/> Human research participants
<input checked="" type="checkbox"/>	<input type="checkbox"/> Clinical data
<input checked="" type="checkbox"/>	<input type="checkbox"/> Dual use research of concern

Methods

n/a	Involved in the study
<input checked="" type="checkbox"/>	<input type="checkbox"/> ChIP-seq
<input type="checkbox"/>	<input checked="" type="checkbox"/> Flow cytometry
<input checked="" type="checkbox"/>	<input type="checkbox"/> MRI-based neuroimaging

Antibodies

Antibodies used

Primary antibodies used in this work include PE/Cy7 rat anti-mouse CD11b antibody (101216, 1:100, Biolegend), PE rat anti-mouse CD163 antibody (156704, 1:100, Biolegend), and APC rat anti-mouse F4/80 antibody (123116, 1:100, Biolegend). For CD31 (ab28364, Abcam), α -SMA (ab5694, Abcam), CD206 (ab64693, Abcam), and CD163 (ab182422, Abcam). DAPI (ab104139, Abcam) was used to stain for nuclei. Secondary antibodies used in this work include Goat anti-Mouse IgG (H+L) Highly Cross-Adsorbed Secondary Antibody, Alexa Fluor Plus 488, A32723, 1:250, Thermo-Fisher; Goat anti-Rabbit IgG (H+L) Highly Cross-Adsorbed Secondary Antibody, Alexa Fluor Plus 647, A32733, 1:250, Thermo-Fisher.

Validation

Validation for primary antibodies can be found on the BioLegend and Abcam websites, including: <https://www.biologend.com/en-us/products/pe-cyanine7-anti-mouse-human-cd11b-antibody-1921?GroupID=BLG10427> for PE/Cy7 rat anti-mouse CD11b, <https://www.biologend.com/en-us/products/pe-anti-mouse-cd163-antibody-19309?GroupID=GROUP564> for PE rat anti-mouse CD163, <https://www.biologend.com/en-us/products/apc-anti-mouse-f4-80-antibody-4071?GroupID=BLG5319> for APC rat anti-mouse F4/80, <https://www.abcam.com/cd31-antibody-ab28364.html> for CD31, <https://www.abcam.com/alpha-smooth-muscle-actin-antibody-ab5694.html> for α -SMA, <https://www.abcam.com/mannose-receptor-antibody-ab64693.html> for CD206, <https://www.abcam.com/cd163-antibody-epr19518-ab182422.html> for CD163, and <https://www.abcam.com/mounting-medium-with-dapi-aqueous-fluoroshield-ab104139.html> for DAPI.

The antibody for PE/Cy7 rat anti-mouse CD11b has been used in previous publications including Myelin oligodendrocyte glycoprotein-specific antibodies from multiple sclerosis patients exacerbate disease in a humanized mouse model in *J Autoimmun*, PMID: 28964723; A Three-Day Consecutive Fingolimod Administration Improves Neurological Functions and Modulates Multiple Immune Responses of CCI Mice in *Mol. Neurobiol.*, PMID: 27924525; and Inhibition of Endosteal Vascular Niche Remodeling Rescues Hematopoietic Stem Cell Loss in AML in *Cell Stem Cell*, PMID: 29276143.

The vendor for the antibody for PE rat anti-mouse CD163 did not provide information about its prior use in publication. We validated the efficacy of the antibody according to the vendor's instruction.

The antibody for APC rat anti-mouse F4/80 has been used in previous publications including Macrophages produce IL-33 by activating MAPK signaling pathway during RSV infection in *Mol Immunol*, PMID: 28531812; Differential expression of Cathepsin E in transthyretin amyloidosis: from neuropathology to the immune system in *J Neuroinflammation*, PMID: 28583160; and Dectin-2 is a primary receptor for NLRP3 inflammasome activation in dendritic cell response to *Histoplasma capsulatum* in *PLoS Pathog*, PMID: 28671985.

The antibody for CD31 has been used in previous publications including Stem Cell/Oxygen-Releasing Microparticle Enhances Erectile Function in a Cavernous Nerve Injury Model in *Tissue Eng Part A*, PMID: 32122268; Construction and Optimization of an Endometrial Injury Model in Mice by Transcervical Ethanol Perfusion in *Reprod Sci*, PMID: 32939736; and Dilated microvessel with endothelial cell proliferation involves intraplaque hemorrhage in unstable carotid plaque in *Acta Neurochir (Wien)*, PMID: 32995934.

The antibody for α -SMA has been used in previous publications including Photobiomodulation and estrogen stabilize mitochondrial membrane potential in angiotensin-II challenged porcine aortic smooth muscle cells in *J Biophotonics*, PMID: 32888351; Elimination of NF- κ B signaling in Vimentin+ stromal cells attenuates tumorigenesis in a mouse model of Barrett's Esophagus in Carcinogenesis, PMID: 33068426; and Downregulating long non-coding RNA PVT1 expression inhibited the viability, migration and phenotypic switch of PDGF-BB-treated human aortic smooth muscle cells via targeting miR-27b-3p in *Hum Cell*, PMID: 33106979.

The antibody for CD206 has been used in previous publications including Mono-macrophage-Derived MANF Protects Against Lipopolysaccharide-Induced Acute Kidney Injury via Inhibiting Inflammation and Renal M1 Macrophages in Inflammation, PMID: 33145627; Targeting the RNA-Binding Protein HuR Alleviates Neuroinflammation in Experimental Autoimmune Encephalomyelitis: Potential Therapy for Multiple Sclerosis in Neurotherapeutics, PMID: 33200288; and Macrophage polarization in peri-implantitis lesions in *Clin Oral Investig*, PMID: 32886246.

The antibody for CD163 has been used in previous publications including Immune response drives outcomes in prostate cancer: implications for immunotherapy in *Mol Oncol.*, PMID: 33338321; The Paradox Effect of Calcification in Carotid Atherosclerosis: Microcalcification is Correlated with Plaque Instability in *Int J Mol Sci.*, PMID: 33401449; and A partially demineralized allogeneic bone graft: in vitro osteogenic potential and preclinical evaluation in two different intramembranous bone healing models in *Sci Rep.*, PMID: 33649345.

The antibody for DAPI has been used in previous publications including Strain Specific Responses in a Microbead Rat Model of Experimental Glaucoma in *Curr Eye Res.*, PMID: 32842792; The potential use of tideglusib as an adjuvant radio-therapeutic treatment for glioblastoma multiforme cancer stem-like cells in *Pharmacol Rep.*, PMID: 33140310; and Dynamic changes in the systemic immune responses of spinal cord injury model mice in *Neural Regen Res.*, PMID: 32859802.

Validation for secondary antibodies can be found on the Thermo Fisher website, including <https://www.thermofisher.com/antibody/product/Goat-anti-Mouse-IgG-H-L-Highly-Cross-Adsorbed-Secondary-Antibody-Polyclonal/A32723> and <https://www.thermofisher.com/antibody/product/Goat-anti-Rabbit-IgG-H-L-Highly-Cross-Adsorbed-Secondary-Antibody-Polyclonal/A32733>.

The Goat-anti-Mouse antibody has been used in previous publications including Permanent Whisker Removal Reduces the Density of c-Fos+ Cells and the Expression of Calbindin Protein, Disrupts Hippocampal Neurogenesis and Affects Spatial-Memory-Related Tasks in Front Cell Neurosci., PMID: 29867365; Paricalcitol accelerates BACE1 lysosomal degradation and inhibits calpain-1 dependent neuronal loss in APP/PS1 transgenic mice in EBioMedicine, PMID: 31303501; and Nexilin/NEXN controls actin polymerization in smooth muscle and is regulated by myocardin family coactivators and YAP in Sci Rep., PMID: 30158653.

The Goat-anti-Rabbit antibody has been used in previous publications including Region-Specific Reductions in Morphometric Properties and Synaptic Colocalization of Astrocytes Following Cocaine Self-Administration and Extinction in Front Cell Neurosci., PMID: 30147645; Arkadia/RNF111 is a SUMO-targeted ubiquitin ligase with preference for substrates marked with SUMO1-capped SUMO2/3 chain in Nat Commun., PMID: 31417085; and Precise inhibitory microcircuit assembly of developmentally related neocortical interneurons in clusters in Nat Commun., PMID: 28703129.

Eukaryotic cell lines

Policy information about [cell lines](#)

Cell line source(s)

Human Umbilical Vein Endothelial Cells (HUVEC) were obtained from Sigma-Aldrich (catalog #C-12203)

Authentication

According to the vendor, rigid quality control tests are performed for each lot of Endothelial Cells from large vessels. They are tested for cell morphology, adherence rate, and cell viability. Flow cytometric analyses for cell-type specific markers, e.g. von Willebrand Factor (vWF) and CD31, as well as Dil-Ac-LDL uptake assays are also carried out for each lot. Growth performance is tested through multiple passages up to 15 population doublings (PD) under culture conditions without antibiotics and antimycotics.

Mycoplasma contamination

All cells have been tested for the absence of HIV-1, HIV-2, HBV, HCV, HTLV-1, HTLV-2 and microbial contaminants (fungi, bacteria, and mycoplasma).

Commonly misidentified lines (See [ICLAC](#) register)

No commonly misidentified cell lines were used.

Animals and other organisms

Policy information about [studies involving animals; ARRIVE guidelines](#) recommended for reporting animal research

Laboratory animals

8–12-week-old female mice (eC57BL/6J, C57BL/6-Tg(CAG-EGFP)1Osb/J; Jackson Laboratory, Bar Harbor, ME, <http://www.jax.org>) were housed in the Stanford University Veterinary Service Center in accordance with NIH and institution-approved animal care guidelines. Mice within one experiment were of the same strain, batch and birthday.

Wild animals

No wild animals were used in the study.

Field-collected samples

No field collected samples were used in the study.

Ethics oversight

All mouse procedures were approved by the Stanford Administrative Panel on Laboratory Animal Care.

Note that full information on the approval of the study protocol must also be provided in the manuscript.

Flow Cytometry

Plots

Confirm that:

- The axis labels state the marker and fluorochrome used (e.g. CD4-FITC).
- The axis scales are clearly visible. Include numbers along axes only for bottom left plot of group (a 'group' is an analysis of identical markers).
- All plots are contour plots with outliers or pseudocolor plots.
- A numerical value for number of cells or percentage (with statistics) is provided.

Methodology

Sample preparation

On day 5, analysis of murine cells isolated from excisional wounds was performed according to published protocols for flow cytometry on murine tissue⁷. Briefly, tissue was explanted on day 5 from the parabiosis model, then micro-dissected and incubated in serum-free Dulbecco's Modified Eagle Medium (DMEM) with 240 U of collagenase IV per mL for 1 h at 37°C in a rotating oven. Digested tissue was filtered, centrifuged and stained with PE/Cy7 rat anti-mouse CD11b antibody, PE rat anti-mouse CD163 antibody, and APC rat anti-mouse F4/80 antibody (Biolegend, San Diego, CA). 4',6-diamidino-2-phenylindole (DAPI) was used to stain dead cells. Flow cytometry was subsequently performed.

Instrument

BD FACS Aria (Becton Dickinson, San Jose, CA)

Software

Flow cytometry data was analyzed using FlowJo (v. 10.5.3, Becton Dickinson, San Jose, CA).

Cell population abundance

The purity of cells were ensured by FACS sorting and the cell abundance was provided with details in Fig. S38.

Gating strategy

Detailed gate strategies were defined in Fig. S43. Briefly, all cells were first gated for single cells excluding duplets, followed by gating for live, DAPI-negative cells. Subsequently, live cells were gated for GFP and macrophages were identified among the GFP+ cells by gating for PE-Cy7-CD11b+ cells. Further, M2 macrophages were subset from all macrophage by gating for PE-CD163+ cells.

Tick this box to confirm that a figure exemplifying the gating strategy is provided in the Supplementary Information.